2010

Numerical study on mixture formation characteristics in a direct-injection hydrogen engine

Sujith Sukumaran
Iowa State University

Numerical study on mixture formation characteristics in a direct-injection hydrogen engine

by

Sujith Sukumaran

A thesis submitted to the graduate faculty
in partial fulfillment of the requirements for the degree of
MASTER OF SCIENCE

Major: Mechanical Engineering

Program of Study Committee:
Song-Charng Kong, Major Professor
Baskar Ganapathysubramanian
Gap-Yong Kim

Iowa State University
Ames, Iowa
2010

TABLE OF CONTENTS

LIST OF FIGURES

LIST OF TABLES

NOMENCLATURE

Roman Symbols

a	speed of sound
a_p	pressure gradient scaling parameter
A	cell face area
A_0	switch (1 or 0) to turn turbulence on or off
A_n	area of nozzle exit
A_{ps}	area at pseudo-diameter exit
c_2	a constant
$\bar{c}_p$	specific heat at constant pressure for the mixture
C_d	discharge coefficient
d_{eq}	equivalent diameter
d_n	nozzle diameter
D	species diffusivity
D_τ	turbulent diffusivity
$\vec{g}$	acceleration due to gravity
Gr	Grashof Number
h_m	enthalpy of species m
k	turbulence kinetic energy per unit mass
k_1	a constant
k_3	a constant
k_d	a constant
K	kinematic momentum

K_T	thermal conductivity
K_2	a constant
l	turbulent length scale
l_{barrel}	axial distance of Mach disk from the nozzle exit
Δl_j	cell size in j direction
m	species index
$\dot{m}$	mass flow rate
$\dot{m}_{air}$	mass flow rate of air entrained
$\dot{m}_n$	mass flow rate at the nozzle exit
$\dot{M}$	momentum rate
MW_{jet}	molecular weight of jet fluid
N	number of cells
N_p	pressure ratio
P_0	stagnation pressure
P_{ch}	chamber pressure
Q	volume flow rate
r	radial position
R	radius of nozzle exit
Re	Reynolds Number
R_v	radius of vortex head
R_g	gas constant
R_{in}	radius of the inlet boundary
s	cell surface

t	Time
T	Temperature
T_0	stagnation temperature
T_{ps}	temperature at pseudo diameter
$\vec{u}$	velocity vector
$\overline{U}$	average axial velocity at the inlet boundary
U_{CL}	center line axial velocity
U_n	nozzle exit velocity
U_{ps}	axial velocity at pseudo diameter plane
V	volume
V_v	velocity of vortex head
Y	fuel mass fraction
z	axial distance from nozzle diameter or equivalent diameter
Z_t	jet penetration

Greek Symbols

α	a constant
α_r	refinement threshold for fuel mass fraction
β_r	refinement threshold for fuel mass fraction gradient
γ	ratio of specific heat of jet fluid
Γ	scaling constant for jet penetration
$\delta_{1/2}$	radial distance of half velocity point
ϵ	turbulent dissipation rate
η	non dimensional radial distance

π	a constant (= 3.1415926)
ρ	Density
$\bar{\rho}$	mixture density at inlet boundary
ρ_{ch}	density of fluid in the chamber
ρ_{calib}	chamber gas density at atmospheric pressure and temperature
ρ_g	density of injected fluid
ρ_m	density of species with index m
ρ_n	density of injected gas at nozzle exit
ρ_{ps}	density of injected gas at pseudo diameter exit plane
$\vec{\sigma}$	viscous stress tensor
T	standard deviation of fuel mass fraction gradient

Subscripts

0	stagnation condition
air	entrained air
c	Cell
ch	chamber
CL	Centerline
eq	mach disk location
g	gas jet
in	inlet boundary
j	coordinate direction
m	species index
n	nozzle exit

ps	pseudo-diameter exit
ref	reference location

Abbreviations

AMR	Adaptive Mesh Refinement
ATDC	after top-dead-center
BTDC	before top-dead-center
CFD	Computational Fluid Dynamics
EVC	exhaust valve close
EVO	exhaust valve open
FEM	Finite Element Method
FVM	Finite Volume Method
IVC	intake valve close
IVO	intake valve open
KIVA	A CFD code developed at Los Alamos National Laboratory
KIVA-4	Version 4 of KIVA
RPM	reciprocation per minute
SOI	Start of Injection

ACKNOWLEDGEMENTS

First and foremost, I would like to express my sincere gratitude to my advisor Prof. Song-Charng Kong for the continuous support he has rendered throughout my MS study. His guidance, motivation, enthusiasm, knowledge and patience helped me to complete the research and writing this thesis. His thorough reviews on my papers and thesis also helped me greatly improve my writing skills. This thesis would not have been possible without his guidance.

Besides my advisor, I would like to thank the rest of my committee, Prof. Baskar Ganapathysubramaniyan and Prof. Gap-Yong Kim being in my committee. I am indebted to Dr. Yuanhong Li, my labmate, for all the help on AMR and KIVA-4. I am also thankful to Dr. Jaal Ghandhi of University of Wisconsin-Madison for providing the multi-jet experimental data. I would also like to acknowledge the financial support of Ford Motor Company for this research.

Heartfelt thanks goes especially to my parents and the rest of my family for their endless love and support, which always have been an essential part of my life. I thank all my friends for their constant help and support.

Last but not least, I am thankful to God for guiding my life through all tests.

ABSTRACT

Numerical modeling of direct hydrogen injection and in-cylinder mixture formation is performed in this paper. Numerical studies on direct-injection hydrogen engines are very limited due mainly to the complexity in modeling the physical phenomena associated with the high-velocity gas jet. The high injection pressure will result in a choked flow and develop an underexpanded jet at the nozzle exit, which consists of oblique and normal shock waves. A robust numerical model and a very fine computational mesh are required to model these phenomena. However, a very fine mesh may not be feasible in the practical engine application. Therefore, in this study a gas jet injection model is implemented into a multidimensional engine simulation code to simulate the hydrogen injection process, starting from the downstream of the nozzle. The fuel jet is modeled on a coarse mesh using an adaptive mesh refinement algorithm in order to accurately capture the gas jet structure. The model is validated using experimental and theoretical results on the penetrations of single and multiple jets. The model is able to successfully predict the gas jet penetration and structure using a coarse mesh with reasonable computer time. The model is further applied to simulate a direct-injection hydrogen engine to study the effects of injection parameters on the in-cylinder mixture characteristics. The effects of the start of fuel injection, orientation of the jets, and the injector location on the mixture quality are determined. Results show that the hydrogen jets impinge on the walls soon after injection due to the high velocity of the gas jet. The mixing of hydrogen and air takes place mainly after wall impingement. The optimal

injection parameters are selected based on the homogeneity of the in-cylinder mixture. It is found that early injection can result in more homogeneous mixture at the time of ignition. Results also indicate that it is more favorable to position the injector near the intake valve to take advantage of the interaction of hydrogen jets and the intake flow to create a more homogeneous mixture.

CHAPTER 1 INTRODUCTION

1.1 Motivation

Fossil fuel has been the basis of today's energy and transport system. However, it is depleting at a fast rate, and its demand increases rapidly with the growth of the world population and industries. Therefore, more reliable sources are required for the future energy needs. On the other hand, the pollution generated by fossil fuel combustion is a serious concern. The greenhouse effects of carbon dioxide are proven to affect the climate adversely [1]. In addition, for many countries, it is also necessary to reduce the dependence on imported oils to improve the nation's economic security. Alternative fuels can be one of the solutions to the above problems. Hydrogen is one of the attractive candidates among the alternative fuels, and its advantages as an engine fuel has been reviewed [2–4]. The U.S. Department of Energy and Department of Transportation have taken initiatives to shift towards a hydrogen-based transportation system. Whether hydrogen will be used in combustion engines or fuel cells in the future depends decisively on the extent to which both concepts meet the existing customer requirements with regard to driving performance, procurement and operating costs. It is believed that the utilization of hydrogen as a fuel for transportation is more likely to be expected in internal combustion engines than in fuel cells at least for some decades [5].

The advantages of using hydrogen as the combustion fuel are many. In contrast to the carbon-based fuels, hydrogen combustion does not produce carbon dioxide or any hydrocarbons. Hydrogen combustion in air is relatively clean as it

results in only water vapor and traces of nitrogen oxides. Furthermore, hydrogen produced from renewable sources such as electrolysis using the off-peaked electricity generated by wind turbines can, in principle, avoid any carbon-related emissions. The high flame speed and low spark energy can make hydrogen combustion more efficient than the conventional fuels. Besides, it has wide flammability limits and the combustion can occur even in very lean mixtures. Other advantages that help hydrogen as a fuel are the higher auto ignition temperature and high diffusivity. These advantages of hydrogen over other fuels can pave the way to hydrogen-fueled internal combustion engines.

Hydrogen has been used extensively in the space vehicles. The high energy-to-weight ratio makes hydrogen a favorite as a rocket propellant. Liquid hydrogen is the fuel of choice for rocket engines, and has been utilized in the upper stages of launch vehicles in many space missions including the Apollo missions to the moon, Skylab, the Viking missions to Mars and the Voyager mission to Saturn. The research on hydrogen engines on ground vehicles can be traced back to 1979 when BMW developed the first generation of hydrogen vehicles powered by a hydrogen engine with a liquid hydrogen tank [6]. In the early research, backfire and pre-ignition problems were found to be prominent and even caused doubts in hydrogen as a viable fuel [7]. Recently direct injection has been shown to significantly reduce or eliminate these combustion anomalies and is currently a primary focus in the development of the hydrogen engine [8].

Experimental research of hydrogen engine combustion has been performed in numerous studies. Das et al. [9] evaluated the potential of using hydrogen for

small horsepower spark-ignition (SI) engines and compared hydrogen fueling with compressed natural gas (CNG). Das [10] determined the performance, emissions, and combustion characteristics of hydrogen-fueled SI and compression-ignition (CI) engines. Li and Karim [11] investigated the onset of knock in a hydrogen-fueled SI engine. Effects of compression ratio, equivalence ratio, and engine speed on the performance and combustion characteristics of a direct-injection SI engine using hydrogen was also investigated by Mohammadi et al. [12]. Effects of the injector location and nozzle design on the efficiency and emissions of a direct-injection hydrogen engine were studied by Wallner et al. [13].

It is critical to understand the physical process of mixing between the injected fuel and the air within the cylinder in order to optimize the overall performance of the direct-injection engine. The high pressure injector used for the direct-injection engines usually have multiple holes in the nozzle tip in order to provide an even distribution of fuel and promote proper mixing. This results in the formation of multiple underexpanded jets in the cylinder, which interact with each other and with the in-cylinder boundaries to form the fuel-air mixture before combustion. Mixture formation in a direct-injection hydrogen engine was studied recently using chemiluminescence imaging [14]. The mixture formation of hydrogen jet was also studied using Schlieren visualization by Peterson and Gandhi [15]. On the other hand, due to the difficulty in modeling the complex physical phenomena and the massive computational need, numerical simulations of direct-injection hydrogen engines are relatively rare.

The high-pressure hydrogen injection will result in an underexpanded supersonic jet at the nozzle exit. This underexpanded jet is characterized by the existence of a barrel-shaped shock and a normal shock, called the Mach disk [16]. It requires a very robust computational fluid dynamics (CFD) code and a very fine computational mesh to resolve these complex shock structures. However, a fine computational mesh is not desired in the practical engine simulation due to its high computational demand. Thus, it is preferable to make use of an underexpanded jet model on a coarse mesh without a significant loss in the physical reality and numerical accuracy.

1.2 Objective

The objective of this study is to use an underexpanded jet model to simulate hydrogen injection and compare the mixture formation inside an engine under different injection conditions. The underexpanded jet model is used to model the supersonic region. The outlet conditions from the underexpanded jet model are used as the inlet for the computational domain. A coarse mesh with an adaptive mesh refinement algorithm is used to capture the hydrogen jet. The evolution of the hydrogen jet and fuel-air mixing process are modeled using a CFD code. In this study, the injection timing, orientation of gas jets, and injector location are varied, and the mixture distribution in the cylinder is analyzed. It is hope that an accurate and efficient computational model can be developed and used as a tool for the design and optimization of direct-injection hydrogen engine to reduce the use of hydrocarbon fuels.

CHAPTER 2 LITERATURE REVIEW

2.1 Overview of Gas Jet Phenomena

Jet flow occurs when a stream of one fluid mixes with a surrounding medium, at rest or in motion. Such flows occur in a wide variety of situations, and the geometries, sizes, and flow conditions cover a large range. This section discusses about the details of jet structure and modeling of a jet.

2.1.1 Steady Jets

In a direct-injection engine, the fuel injector issues fuel jets which propagates across the combustion chamber. Understanding the physics of the gas jet is necessary to model the fuel jet injected into an engine cylinder. Although the main concern with automotive injection is the transient behavior, steady jets provide a basis for understanding the structure and scaling of the transient jet. The behaviors of steady state jets are discussed in this section.

2.1.1.1 Incompressible Jets of Uniform Density

The compressibility effects in a flow can be neglected if the maximum Mach number is below 0.3. Incompressible jets have been studied extensively in the past [17-19]. As one fluid is injected into another fluid with uniform pressure field, a mixing layer is formed between the two fluids. Mass from the surrounding fluid is entrained in the injected fluid. Experimental investigations by Ricou and Spalding [17] concluded that, the rate of entrainment is proportional to the distance from the nozzle and to the mass injection rate for incompressible air jets issued from the round nozzle into stagnant air. The mass flow rate $\dot{m}$ at the cross-section of the jet is found to be

$$\frac{\dot{m}}{\dot{m}_n} = 0.32\frac{z}{d_n} \tag{2.1}$$

where $\dot{m}_n$ is the mass flow rate at the nozzle, z is the distance from the nozzle and $d_n$is the nozzle diameter. The mass entrainment rate was found to be independent of the nozzle Reynolds number for Reynolds number greater than $3x10^4$.

A steady-state jet can be divided into three regions [20]. In the initial region the velocity in the potential core of the jet remains constant and is equal to the initial velocity. The end of the initial region is marked by the disappearance of the potential core because of the thickening of jet boundary layer. The transition region may be defined as the region in which the jet viscosity distribution becomes fully developed. In the fully developed region, the velocity profile is self-similar. The linearity of the increase in jet thickness can be derived theoretically. In the fully developed region the radial velocity profile, U(r,z), normalized by the centerline velocity, $U_{CL}(z)$, is only a function of the dimensionless distance, η = r/R , where z is the axial distance from the nozzle exit, r is the radial position and R is the radius of the nozzle exit. These relations are represented in Eq. (2.2).

$$\frac{U(r,z)}{U_{CL}(z)} = f(\eta) \tag{2.2}$$

The centerline velocity in the jet can be obtained as a function of the distance from the nozzle. For example, the centerline velocity decay of a round jet can be expressed by

$$\frac{U_{CL}}{U_n} = \frac{k_d}{(\frac{z}{d_n})} \tag{2.3}$$

where U_n is the flow velocity at the nozzle exit, and k_d is a constant that has been experimentally been determined to be approximately 5.0 [19,21]. As seen in Eq.

(2.3), the centerline velocity scales with the inverse of distance from the exit plane. The velocity profile of the steady jet can be derived from the continuity and momentum conservation equations using the boundary layer simplifications [22]. The volume flow rate of fluid at a distance, z from the orifice can be calculated from the velocity profile as

$$Q = 0.404\sqrt{K}\,z \tag{2.4}$$

where K is the kinematic momentum, which is given by

$$\sqrt{K} = 1.59\delta_{1/2}\mathrm{U_{CL}}\,. \tag{2.5}$$

$\delta_{1/2}$ is the radial distance of the half-velocity point,

$$\delta_{1/2} = 0.848\mathrm{z}\,. \tag{2.6}$$

The above equations provide a complete description of the velocity profile in the fully developed part of turbulent jets.

2.1.1.2 Incompressible Jets of Different Densities

When the densities of the injected fluid and surrounding fluid are different, the entrainment rate is different from that determined using Eq. (2.1). The centerline velocity is also different in this case. However, the similarity of the profiles in the jet is still preserved at some distance from the nozzle. It is confirmed experimentally [17] that jets of different densities can be scaled when an equivalent diameter as defined in Eq. (2.7) is used.

$$d_{eq} = d_n\left(\frac{\rho_g}{\rho_{ch}}\right)^{\frac{1}{2}} \tag{2.7}$$

In the above equation, ρ_g and ρ_{ch} are the injected fluid and surrounding fluid densities respectively, taken at the same pressure. Thus, incompressible jets of different densities can be modeled by replacing the nozzle diameter in Eq. (2.1) and (2.3) by the equivalent diameter. This modification is directly obtainable from momentum conservation and similarity arguments. The difference in density may be the result of different molecular weights or of different temperature, or both.

2.1.1.3 Compressible Jets

As the pressure ratio across the nozzle is increased, the velocity at the nozzle increases. As the Mach number increases above 0.3, compressibility effects have to be taken into account in establishing nozzle exit conditions. The similarity of profiles is still valid in the fully developed region where the local Mach numbers are low. However, the effect of compressibility on the nozzle density and velocity must be incorporated in the scaling. A logical modification to the equivalent diameter proposed in the previous section can be used to incorporate these effects. The equivalent diameter is calculated as shown in Eq. (2.8)

$$d_{eq} = d_n \left(\frac{\rho_n}{\rho_{ch}}\right)^{\frac{1}{2}} \tag{2.8}$$

where ρ_n is the nozzle exit density.

When the upstream to the chamber pressure ratio is greater than the critical pressure ratio for hydrogen jet, the exit plane pressure of the nozzle becomes higher than the chamber pressure, and an underexpansion occurs. An underexpanded jet consists of a complex structure of expansion waves and compression waves. The expansion waves reflect from the free boundary of the jet and become compression shocks that form a barrel shaped structure that is terminated by a normal shock also

called the Mach disk [16]. The Mach disk forms if the nozzle exit to chamber pressure ratio is above 2.1 [23]. Figure 2.1 shows a schematic of the expansion process outside the nozzle.

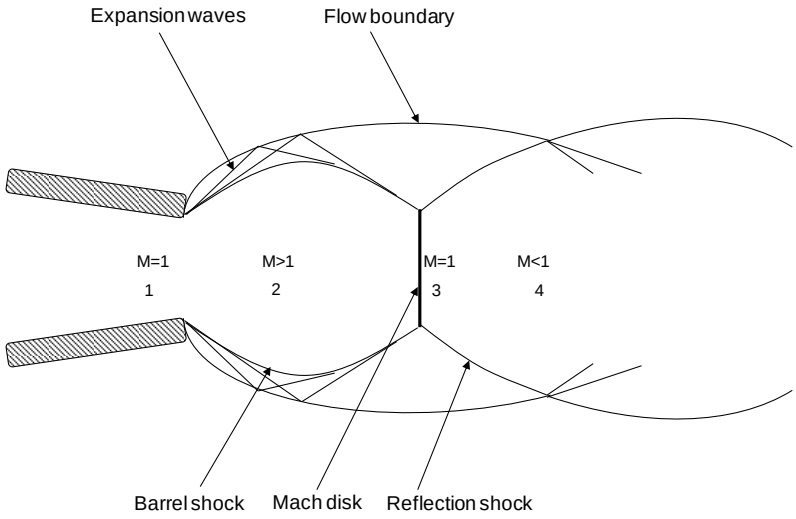

Figure 2.1 Schematic of underexpanded jet

Ewan and Moodie [24] and Birch et al. [25] proposed a pseudo-diameter model similar to the classical jet model. The pseudo-diameter correction was found to scale the experimental data by these authors. Based on the assumption that no mixing takes place in the underexpansion region, mass conservation is used to provide an equivalent diameter.

$$\frac{A_{ps}}{A_n} = \frac{C_d \rho_n U_n}{\rho_{ps} U_{ps}} \tag{2.9}$$

where the subscript ps and n refer respectively to conditions at the pseudo-diameter exit plane and at the nozzle exit. C_d is the discharge coefficient. The nozzle conditions can be calculated from one-dimensional flow, which can include frictional effects and real gas behavior. As the nozzle is choked, the nozzle Mach number M_n is unity. Pseudo-diameter conditions are obtained by Ewan and Moodie [24] and Birch et al.

[25] by assuming that M_{ps} is unity at the pseudo-diameter. Another assumption used in the analysis is that the temperatures at the pseudo-diameter exit and nozzle exit are the same. This assumption is supported by the previous assumptions that no mixing occurs in the expansion region and the Mach number at both the locations are same. The density at the equivalent exit plane is given at the temperature prescribed from the unity Mach number and from the exit plane pressure which must be the chamber pressure. If ideal gas law is assumed, and based on the above assumptions, the velocities U_n and U_{ps} are the same, and the pseudo-diameter becomes

$$\frac{d_{ps}}{d_n} = \sqrt{C_d \left(\frac{\rho_n}{\rho_{ps}}\right)} \tag{2.10}$$

In Ewan and Moodie [24] and Birch et al. [25], the nozzle density is obtained from the upstream conditions assuming ideal gas law and isentropic one-dimensional flow through a choked nozzle,

$$\rho_n = \frac{P_0}{R_g T_0}\left(\frac{2}{\gamma+1}\right)^{1/(\gamma-1)} \tag{2.11}$$

The pseudo-diameter density is

$$\rho_{ps} = \frac{P_{ch}}{R_g T_{ps}} = \frac{P_{ch}}{R_g T_0}\left(\frac{\gamma+1}{2}\right) \tag{2.12}$$

where the assumption of constant stagnation temperature has been used. Thus, Eq. (2.8) can be written as

$$\frac{d_{ps}}{d_n} = \sqrt{C_d \left(\frac{2}{\gamma+1}\right)^{\frac{\gamma}{\gamma-1}} \left(\frac{P_0}{P_{ch}}\right)}. \tag{2.13}$$

Both Ewan and Moodie [24] and Birch et al. [25] confirmed that the experimental data could be scaled well using the pseudo-diameter instead of the nozzle diameter.

Ewan and Moodie [24] included the correction of Eq. (2.7) for compressibility effects in the length scale, replacing ρ_n by ρ_{ps}. The equivalent diameter used was then of the form,

$$d_{eq} = d_n(\frac{\rho_{ps}}{\rho_{ch}})^{1/2} \left[C_d \left(\frac{2}{\gamma+1}\right)^{\frac{\gamma}{\gamma-1}} \left(\frac{P_0}{P_{ch}}\right)\right]^{1/2} \quad (2.14)$$

where the first nozzle diameter modifier takes into consideration, effects of compressibility and different densities, and the second modifier takes into account the underexpansion. The equivalent diameter of Eq. (2.14) should be applicable to all turbulent jets issued from converging round nozzles. The equivalent diameter can be used with Eq. (2.1) and (2.3) to model the jet flow in the case of an underexpanded jet. Ewan and Moodie [24] also provided a correlation between the barrel length, l_{barrel}, exit diameter, d_n, and the nozzle exit to ambient pressure ratio, N_p, given in Eq. (2.15).

$$l_{barrel} = 0.77d_n + 0.068\, d_n^{1.35}\, N_p. \quad (2.15)$$

2.1.2 Transient Jets

The structure and properties of incompressible transient jets or impulsively started jets have been studied for a wide range of applications. Turner [26] described the structure of plumes when studying atmospheric mixing in buoyant plumes. A plume was described as consisting of a spherical cap, called a spherical head vortex, which is supplied with additional buoyancy and momentum from a plume below. It was shown that the plume displays self-similarity characteristics throughout its evolution. Figure 2.2 illustrates this initial description of a jet or plume. The jet consists of a spherical vortex flow interacting with a steady-state jet. The vortex of

radius R_v moves away from the nozzle at a bulk velocity that decays with the distance z from the nozzle. The size of the vortex grows continuously due to the entrainment of mass from the steady-state jet which pushes it from behind. The jet behind the vortex is considered to be in a steady state, which is confirmed by the work of Kuo and Bracco [27].

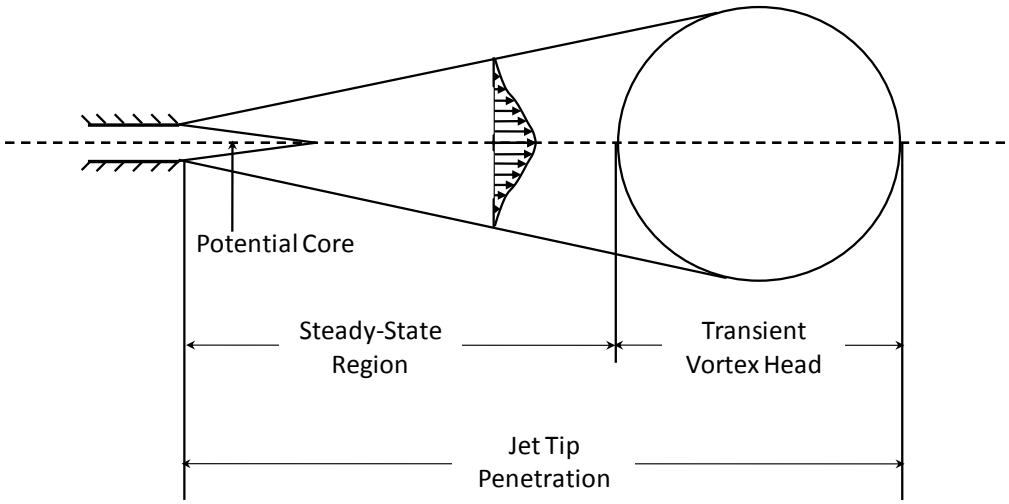

Figure 2.2 Turbulent transient jet model

Turner's plume was used as the basic structure of a transient starting jet by many subsequent authors. Abramovich and Solan [28] used this model to develop analytical expressions for the velocity of the spherical vortex in the near and far fields of a liquid jet under laminar conditions with low Reynolds number. It was observed that the velocity of the spherical vortex varies proportional to the distance similar to the axial velocity of a steady state jet only with differing constants. The velocity of the spherical vortex was found to be approximately half that of a fluid element in a steady jet. Abramovich and Solan [28] showed that the half width and maximum axial velocity show similarity characteristics, both making the jet appear to start from a virtual origin different from the geometric origin. The virtual origin was

found to be proportional to the exit diameter and the square root of the Reynolds number. A previous study by Sato and Sakao [29] also found that an offset or virtual origin was needed to obtain agreement between experiment and theory with the origin moving downstream with increasing Reynolds number.

Hill and Ouellette [30] reviewed the self-similar characteristics of transient turbulent jets and developed an analytical relationship for the penetration. From the transient jet visualization performed by Miyake et al. [31], it was found that the radius R of the vortex head is a constant function of the distance from the nozzle, z.

$$R_v = K_2 z\,. \tag{2.16}$$

K_2 is approximately 0.28.

In the case of transient jets issued from round nozzles, the total momentum of the vortex head can be taken as a fraction of the total momentum injected,

$$\dot{M}t = k_1 \rho \pi {R_v}^3 V_v \tag{2.17}$$

where $\dot{M}$ is the momentum rate at the nozzle, k_1 is a proportionality constant and ρ, R and V_v are average density, radius and velocity of the vortex head.

The velocity of the vortex head can be written as,

$$V_v = k_3 \frac{dz}{dt} \tag{2.18}$$

where k_3 is a proportionality constant of the order of 1, and *z,* is the distance of the vortex head front from the nozzle. From Eq. (2.15), (2.16) and (2.17), it was derived that

$$z \propto t^{1/2}. \tag{2.19}$$

Hill and Ouellette [30] also employed the Turner model [26] to approximate the geometry of a gas jet. In their model the jet is constantly supplied with

momentum through the orifice, and the momentum is, in turn, passed between the quasi-steady jet and the head vortex. The entrainment of the low momentum ambient fluid was assumed to follow the relationship reported by Ricou and Spalding [17]. The jet penetration was assumed, based on dimensional grounds, to follow the form,

$$\frac{Z_t}{d_{eq}} = \alpha \left(\frac{tu_n}{d_{eq}}\right)^{1/2}. \tag{2.22}$$

$$\alpha = \Gamma \left(\frac{\pi}{4}\right)^{1/4}. \tag{2.21}$$

The scaling constant Γ was found to be approximately equal to 3.0. Similar scaling approach was used for jet penetration by others [32-34]. The reported values of α differ in the literatures.

2.2 CFD Modeling of Gas Jets

CFD modeling of the transient injection of gaseous hydrogen and its combustion in a constant volume chamber was done by Johnson et al. [35]. The nozzle flow exit conditions were calculated using a pilot simulation of fluid dynamics in the neighborhood of nozzle. The model predictions were compared with experimental results on penetration. It was shown that the penetration of hydrogen under combustion conditions is comparable to the penetration without combustion. The flow structure of an underexpanded jet under high-pressure injection was studied and also modeled using a fine computational grid near the orifice by Li et al. [36]. The Mach disk structures were demonstrated in the experiment. Hill and Oulette [30] also developed a CFD model to approximate an underexpanded jet as a perfectly expanded jet with an enlarged initial diameter to match the mass flow rate.

It was also noted that by assuming the flow is isothermal near the nozzle exit, the momentum flux is conserved between the two jets. Their simulation showed fair agreement with data collected by Witze [19], especially at later times in the injection. A very fine grid size adjacent to the nozzle was suggested by Hill and Oulette [30].

Ra et al. (2005) [37] also performed numerical simulations of transient underexpanded jets. They first approximated properties of the underexpanded jet in the same manner, a larger sonic jet with the same mass flow at the location of the Mach disk. The flow was further approximated by integrating the centerline velocity equation of an incompressible jet given by Schlichting [22] to produce inflow boundary conditions for the simulation, reducing the massive change in length scales. This method was found to produce good results when compared to experimental data and theoretical relations.

2.3 Adaptive Mesh Refinement

In order to achieve accurate results for the numerical solution of Navier-Stokes equations, the grid resolution needs to be fine enough to resolve the physical scales of the problem. However, a very fine mesh all over the domain is not a practical approach as it requires enormous computational time to solving such a mesh. A static mesh with a fine discretization at the regions where high gradient flow features are expected can be used for simple problem. But this method may not be applicable to most of the engineering problems, as the flow features are not known before the simulation is performed. Adaptive Mesh Refinement (AMR) techniques have proven helpful in such cases. AMR utilizes the solution on a coarse grid to

dynamically refine the mesh so that the subsequent iterations are performed on a grid with desirable mesh density. The mesh refinement methods are generally characterized as r-refinement, h-refinement and p-refinement.

In r-refinement, the mesh is modified by clustering nodes at the regions of high activity. Enrichment indicators are used determine the mesh density required at each region. This enrichment criterion is a weighing function, which has a very large value where high grid resolution is required and a small value elsewhere. A standard weighing function could be a primitive variable, a derived quantity or any identifiable quantity of the solution which required high resolution. The increase in resolution is made by moving the grid points into regions of activity. Thus the r-refinement of a mesh does not vary the number of nodes or cells present in a mesh or the connectivity of a mesh. The movement of the nodes can be controlled in various ways. On common technique is to treat the mesh as if it is an elastic solid and solve a system of equations that deforms the original mesh subject to some force. The main advantage of this refinement is that the number of grid points remains constant and hence the required computational resources also will be constant. The disadvantage is that, as the nodes move the skewness of the cell might increase. Also the surface geometry is not preserved if the nodes on the surface are translated.

In p-refinement the order of numerical approximation is varied locally. The initial mesh is kept the same, but the order or accuracy of the polynomial in each cell is varied based on the solution. One of the most important advantages of p-refinement is the ability to produce the exponential decay of the discretization error for sufficiently smooth solutions. The effectiveness of p-refinement also depends on

the number of elements and its uniformity, the form of geometric singularities and the discontinuities in the boundary conditions. The fast convergence of p-refinement is achieved at the expense of significantly increased computational cost. This method is a very popular tool in Finite Element Modeling (FEM) rather than in Finite Volume Modeling (FVM).

In h-refinement is the modification of mesh resolution by adding more nodes in the regions where a high accuracy is required. The simplest strategy for this type of refinement subdivides cells. In this case, every parent cell is divided into child cells. The advantage of such a procedure is that the overall mesh topology remains the same. An additional point to be noted is that this type of mesh adaptation can lead to what are called hanging nodes. In 2D, this happens when one of the cells sharing a face is divided and the other is not, as shown below. For two quad cells, one cell is divided into four quads and other remains as it is. The hanging node is depicted in Figure 2.3 as the highlighted node.

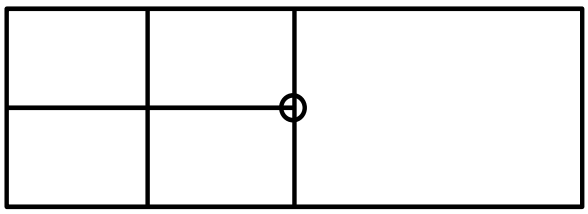

Figure 2.3 Hanging Node in an h-refinement

This leads to a node on the face between the two cells which do not belong (properly) to both of the cells. In the above case, the topology seemingly remains same, but the right (undivided) cell actually has five faces. Thus additional numerical procedures have to be implemented in the solution method in order to transfer flux between the divided and undivided cells.

One can decrease the error in the solution on a computational mesh by increasing the number of nodes in the mesh. It has been shown that the error decreases when the number of nodes is increased in a regular mesh. However, in the case of an irregular mesh, the addition of nodes must be selective, since the distribution is not less important than the number of nodes. The precision of the finite difference operators depends on the quality of the node clouds. In order to avoid ill conditioning clouds, a limit used for the minimum distance between nodes. New node should not be added if the distance between the new node and any existing node is less than this limit. The minimum limit is an important parameter for h-refinement and is given as the maximum distance between any two nodes of the mesh multiplied by a positive parameter. H-refinement does not have all the other disadvantages mentioned in the other types of refinement and is flexible to apply to a multi-dimensional CFD code. It is also less difficult to implement h-refinement and use it with sub-models in a multidimensional CFD code.

The goal of adaptive mesh refinement is to refine the mesh at selected regions alone based on certain criterion. However, it is to be remarked that AMR does not only encompass division of cells into smaller ones (Refinement), but also the agglomeration of smaller cells into a larger one (De-refinement or coarsening), when the need arises.

CHAPTER 3 MODEL FORMULATION

3.1 Base CFD Code with AMR Algorithm

The collocated version of the KIVA-4 code [38] was used as the baseline computer code in this study. KIVA-4 [39] is an unstructured version of the KIVA code family. The new unstructured capability of the code allows the flexibility of mesh generation for more complicated geometries with high mesh quality. This new feature also provides a platform for implementations of other capabilities (such as Adaptive Mesh Refinement (AMR) and Multigrid). KIVA-4 solves the conservative equations closed by a Reynolds-Averaged Navier-Stokes (RANS) turbulence model for the gas phase. The spray injection and chemical reaction models are not used in this study. The conservation equations are written in the integral form as follows.

Conservation of species:

$$\frac{D}{Dt}\int_v \rho_m dV = \int_s \left[\rho D \nabla\left(\frac{\rho_m}{\rho}\right)\right] dA \tag{3.1}$$

Conservation of momentum:

$$\frac{D}{Dt}\int_v \rho\vec{u} dV = \int_s \left[\frac{1}{{a_p}^2} p + A_0 \frac{2}{3}\rho k\right] dA + \int_s \vec{\sigma}.dA + \int_V \rho\vec{g}.dV \tag{3.2}$$

Conservation of energy:

$$\frac{D}{Dt}\int_v \rho I dV = \int_s \left[K_T \nabla T + \rho D \sum_m h_m \nabla\left(\frac{\rho_m}{\rho}\right)\right] dA + \int_V -p\nabla.\vec{u} dV +$$

$$\int_V (1 - A_0)\vec{\sigma}:\nabla\vec{u}.dV + \int_V A_0 \rho\epsilon dV \tag{3.3}$$

Temporal and spatial differencing is performed using the Arbitrary Lagrangian-Eulerian (ALE) technique, which is a semi-implicit quasi second-order upwind approach. An implicit discretization method was used to discretize the terms

of thermodynamic pressure, diffusion of mass, momentum, energy and turbulence. Each discretized equation was solved iteratively using the conjugate residual method. Velocity, temperature and pressure were solved by using the SIMPLE method in an outer iteration in which the pressure field is obtained by simultaneously solving the equations for the linearized equation of state, the cell volume and the face volume change. This code is specifically designed for investigating engine in-cylinder processes, as it is particularly suitable for using moving grids. In order to model the in-cylinder turbulence, a standard k-ε turbulence model is chosen as it is one of the most extensively used and validated turbulence models in engineering application. This model is also adequate in simulating the transient engine in-cylinder flows with reasonable computer time. Turbulent law-of-the-wall velocity conditions with a fixed temperature are used for the wall boundary. In the meantime, the code has been modified by including the AMR algorithm in our previous studies to improve the computational efficiency [40].

Adaptive mesh refinement has been used in liquid spray simulation to increase the spatial resolution and overcome the mesh dependence without incurring a significant computational cost [40, 41]. A similar approach is used in this paper to model the high-speed gas jet with an increased spatial resolution in the vicinity of the gas jet. The original KIVA-4 uses a staggered approach for solving the momentum and density-based equations for compressible flow. A collocated approach, in which velocity is solved at the cell center, is adopted in this study in order to simplify the numerical scheme and the implementation of AMR. Despite that experimental data are not available to verify the predicted in-cylinder flows in

this study, validations of this collocated version of KIVA-4 are reported by Torres [38]. In the above study, the in-cylinder flow results using the collocated version are compared with those using the staggered version. The collocation of pressure and velocity can cause unphysical pressure oscillations [42], but this problem is eliminated by using a pressure correction method [43].

In order to capture the hydrogen jet, a very fine mesh is required in the region where the jet is present. This is achieved using an adaptive mesh refinement algorithm. The current AMR implementation utilizes the data structure and numerical methods based on the features of the KIVA-4 solver. The present approach adds new child cells to the existing cells and uses a hierarchical structure to establish the relationship between the parent cell and its child cells. The cell-centered properties of the child cells are determined using the linear variation with local conservation. The refined cells will be coarsened to reduce the computational cost if a higher grid resolution is not required. These dynamic refinement routines are controlled by using an adaptation criterion based on the fuel mass fraction, Y and its gradients, $\dot{Y}_{c,j}$. The fuel mass fraction criterion could ensure the proper adaptation at region near the injector nozzle. The fuel mass fraction gradients were also chosen in order to provide adequate grid resolution at the jet periphery, where the mass fraction gradients were high. First derivatives were used to calculate the adaptation indicator from the mass fraction gradients as,

$$\dot{Y}_{c,j} = \left|(\nabla Y)_{c,j}\right| \Delta l_j \tag{3.4}$$

where $(\nabla Y)_{c,j}$ is the gradient component of the variable Y at a cell c in j coordinate direction. Δl_j is the mesh size in j direction. Notice that the repeated index does not imply Eisenstein summation. The following conditions were used for the grid adaptation:

(1) If $\dot{Y}_{c,j} > \alpha_r \tau$ in any coordinate direction j, or $Y > \beta_r$, the cell is flagged to be refined.

(2) If $\dot{Y}_{c,j} \leq \alpha_r \tau$ in all coordinate directions and $Y \leq \beta_r$ for all the cells refined from the same parent cell, these cells are to be coarsened. α_r and β_r are the control. τ is the standard deviation calculated as

$$\tau = \left(\frac{1}{3N} \sum_{j=1}^{3} \sum_{c=1}^{N} \dot{Y}_{c,j}^2 \right)^{1/2} \tag{3.5}$$

where *N* is the total number of the active cells. In addition, the difference in the refinement levels at the cell interface was limited to one to ensure a smooth transition in the refinement levels.

3.2 Gas Injection Model

The high pressure hydrogen injection creates a region of underexpanded jet near the injector exit. A schematic of the choked flow underexpansion process has been shown in Figure 2.1. This underexpanded jet is characterized by an oblique shock of a barrel shape, a vertical shock with a disk shape (called the Mach disk), and subsequent reflected shocks. The flow downstream of the Mach disk will become subsonic. A full CFD modeling would start from the nozzle exit and simulate the supersonic flow, shock waves, and subsequent subsonic flow downstream. However, in order to reduce the complexity of the flow simulation in an engine application, a

gas injection model is employed in this study to avoid the simulation of the supersonic flow and shock waves. Since the supersonic flow in the underexpanded region is not simulated in the engine cylinder, only the flow at the downstream of the Mach disk is modeled. The gas jet can be modeled starting from the Mach disk by using a proper inflow boundary to represent the conditions at that location.

It is assumed that the process between the nozzle exit and the Mach disk is isothermal and there is no flow across the barrel shock [30]. Thus, the Mach disk conditions can be calculated as below.

The conditions at each locations of an underexpanded jet are as follows.

1: Upstream or reservoir, P_o, T_o, ρ_o

2: Nozzle exit, choked condition, P_n, T_n, ρ_n, v_n (M=1)

3: Mach disk, P_{eq}, T_{eq}, ρ_{eq}, v_{eq} (M=1)

4: Downstream or chamber, P_{ch}, T_{ch}, ρ_{ch}, v_{ch} (M<1)

The assumptions are $T_n = T_{eq}$, $P_{eq}=P_{ch}$. The mass flow rate, $\dot{m}$ is calculated as

$$\dot{m} = A_n v_n \rho_n = A_{eq} v_{eq} \rho_{eq} \ . \tag{3.6}$$

From the assumption that the gas temperature at the nozzle exit is equal to that at the Mach disk, the gas velocities are same, which are the speed of sound, a, because the Mach number is equal to unity.

$$v_n = v_{eq} = a \ at \ T_n \ . \tag{3.7}$$

The equivalent diameter of the Mach disk can be calculated as

$$\frac{D_{eq}}{D_n} = \sqrt{\frac{P_n}{P_{ch}}}\,. \tag{3.8}$$

The conditions at the nozzle exit are calculated from the reservoir conditions as

$$T_n = \frac{2}{\gamma+1} T_0, \qquad P_n = \left(\frac{2}{\gamma+1}\right)^{\gamma/\gamma+1} P_0 \tag{3.9}$$

where γ is the specific heat ratio of the injected gas.

The conditions at the Mach disk are calculated as

$$T_{eq} = T_n, \;\; P_{eq} = P_{ch}\,, \rho_{eq} = \frac{P_{eq}}{R_g T_{eq}} = \frac{P_{ch}}{R_g T_n} = \frac{P_{ch}}{R_g T_0}\left(\frac{\gamma+1}{2}\right). \tag{3.10}$$

With the above conditions, the flow modeling can start from the downstream of the Mach disk. Nonetheless, this approach will still be computationally expensive as the size of the Mach disk is extremely small, and thus a very fine mesh is required to capture the jet structure. Besides, the size of the Mach disk will change as the pressure inside the chamber changes. Therefore, a new approach is proposed in which the gas jet simulation will start from a location where the size of the jet is comparable to the local computational cell. The details of this approach are explained below.

The downstream conditions at a certain distance from the Mach disk are calculated using appropriate similarity solutions and empirical relations. The size of the Mach disk is assigned as the new nozzle diameter for the similarity solution, and thus the velocity at the new nozzle exit is sonic. At the distance z from the Mach disk, where the jet width ($2R_{in}$) is equal to the size of the inflow boundary of the

computational grid, the flow rate (Q) is calculated from the similarity solution of a turbulent circular jet [22],

$$Q = 0.404\sqrt{K}z\ . \tag{3.11}$$

K is the kinematic momentum, which is given by

$$\sqrt{K} = 1.59\delta_{1/2}U_c\ . \tag{3.12}$$

$\delta_{1/2}$ is the radial distance of the half-velocity point and U_c is the centerline velocity. Calculation of $\delta_{1/2}$ and U_c is discussed in section 2.1.1.1. The average velocity can be calculated as

$$\overline{U} = Q/\pi R_{in}^{\ 2}\ . \tag{3.13}$$

The mass flow rate of the jet is calculated using the empirical correlations by Ricou and Spalding [17],

$$\dot{m}\ = \dot{m}_n(0.32)\frac{z}{d_n(\rho_g/\rho_{ch})^{1/2}} \tag{3.14}$$

where $\dot{m}_{\mathrm{n}}$ is the mass flow rate at the nozzle exit, d_n is the nozzle diameter, ρ_g is the density of injected gas, and ρ_{ch} is the density of chamber gas. Since the correlation is used to link the flow conditions from the Mach disk to the computational inflow boundary, the conditions at the Mach disk is regarded as the starting conditions. In other words, d_n is equal to the Mach disk size D_{eq}, and ρ_g is the gas density at the Mach disk location, ρ_{eq}. The mass flow rate of the entrained air can then be obtained as $\dot{m}_{\mathrm{air}} = \dot{m} - \dot{m}_{\mathrm{n}}$. The composition at inlet boundary is calculated using $\dot{m}_{\mathrm{air}}$ and $\dot{m}_{\mathrm{n}}$.

In order to calculate the average density of the gas mixture at the downstream location, the assumption of complete mixing is used. The average density of the gas mixture is calculated from the mass flow rate and the size of the inflow boundary.

$$\bar{\rho} = \dot{m}/(\pi R_{in}^2 \bar{U}) \tag{3.15}$$

The average temperature of the gas mixture at the downstream location, which is the computational inflow boundary, is obtained using the internal energy balance equation.

$$\dot{m}\bar{c}_p\bar{T} = \dot{m}_{eq}\bar{c}_{p,eq}\bar{T}_{eq} + \dot{m}_{air}\bar{c}_{p,air}\bar{T}_{air} \tag{3.16}$$

$$\bar{T} = \frac{\dot{m}_{eq}\bar{c}_{p,eq}\bar{T}_{eq}+\dot{m}_{air}\bar{c}_{p,air}\bar{T}_{air}}{\dot{m}\bar{c}_p} \tag{3.17}$$

Once the average density of the gas mixture at the downstream location is determined, the composition of the gas mixture is calculated using the flow rates of the injected hydrogen and the entrained air. From the similarity solution [37], the correlation between the axial location and the equivalent jet half width can be obtained as

$$R = 0.22888z \tag{3.18}$$

Thus, the distance of the inflow boundary shift can be calculated using

$$z_{in} = R_{in}/0.22888 \tag{3.19}$$

The inlet boundary conditions for turbulence are also determined using the solution for circular jet. The virtual kinematic viscosity, D_τ, for a circular jet is a constant [21].

From the k-ε turbulence model [44], the turbulent diffusivity or kinematic viscosity is given by

$$D_\tau = c\rho k^{1/2} l = constant \tag{3.20}$$

where *c* is a model constant, *k* is the turbulent kinetic energy, and *l* is the turbulence length scale. Thus,

$$\rho_{ref} k_{ref}^{1/2} l_{ref} = \rho_{in} k_{in}^{1/2} l_{in} \tag{3.21}$$

where the reference location, *ref*, is at the nozzle exit or at the Mach disk location in the case of the underexpanded jet. The subscript *in* refers to the inlet boundary. The turbulent kinetic energy at the inflow boundary location, k_{in}, is thus calculated as

$$k_{in} = c_2 k_n \left(\frac{\rho_{ref} l_{ref}}{\rho_{in} l_{in}}\right)^2 \tag{3.22}$$

Where c_2 is a model constant, k_n denotes the turbulent kinetic energy at nozzle exit, which is normally about 10 % of jet kinetic energy. For the case of underexpanded jets, ρ_{ref} is the density Mach disk and l_{ref} is the Mach disk diameter. ρ_{in} and l_{in} are calculated as the average density, $\bar{\rho}$ and the radius at the inlet boundary, R_{in}. The value of c_2 is given by Eq. (3.23), determined using numerical calibration [37].

$$c_2 = \left(\frac{6}{MW_{jet}}\right)^2 \left(\frac{\rho_{calib}}{\rho_{ch}}\right) \tag{3.23}$$

where MW_{jet} is molecular weight of the gas jet and ρ_{calib} is chamber gas density at standard atmospheric pressure and temperature. The turbulent length scale at the inlet boundary is specified as the radius of inlet boundary R_{in}.

3.3 Integration of Gas Injection with AMR Algorithm

A study on the grid dependence is first conducted in this study. A cylindrical domain of 5 cm in diameter and 10 cm in height is used for this purpose. Hydrogen is injected from the center of the top surface. The nozzle diameter is 250 μm. The injection pressure is 207 bar and the chamber pressure is 62 bar. The temperatures at the injector and chamber are 450 K and 1150 K, respectively. Three different computational grids used are labeled as R1 (15x15x30 cells), R2 (30x30x60 cells), and R3 (60x60x120 cells). As shown in Figure 3.1, it can be seen that the gas penetrations after 1 ms are similar for all the cases. However, the R1 grid results in a higher diffusion of the hydrogen jet compared to the other two cases. As a result, an unphysical jet shape is predicted using the coarse mesh. This will cause an underpredicted penetration at a later time. The computer time required for the above cases is 0.63 hours, 5.47 hours and 101.2 hours for R1, R2, and R3 grids, respectively, at 1 ms after the start of injection. While it is generally agreed that a finer mesh can potentially result in more accurate simulations and detailed flow structures, the long computer time associated with the fine mesh needs to be avoided. One approach is to use the AMR algorithm. By dynamically generating a fine mesh in the region of the gas jet, it is possible to accurately capture the jet structure without incurring significant computer time.

A two-level AMR algorithm is used in this study to model the hydrogen jet. Both the hydrogen mass fraction and its mass fraction gradients are used as the refinement criteria. The cell is set to be refined if the mass fraction of hydrogen exceeds a certain threshold (β_r) or the mass fraction gradient exceeds a certain

fraction (α_r) of the standard deviation of the mass fraction gradient. The mass fraction criterion is used to adapt the cells in the core region of the hydrogen jet where the hydrogen jet convection is prominent due to the high velocity. The mass fraction gradient criterion is used to adapt the cells at the boundaries of the hydrogen jet where diffusion is prominent. In all the simulations described in this paper, α_r and β_r are set as 0.75 and 0.33, respectively. These values are chosen based on the sensitivity study and the consideration of the simulation accuracy and the computational cost. If a smaller value is used, a large number of cells will be refined, resulting in longer run time. If a larger value is used, less number of cells will be refined, which does not provide the benefits of grid refinement. The above values were selected after running the tests on single jet with different values for these criteria. These values are somewhat empirical and different numerical values have been used in different applications (e.g., liquid spray simulation [40]).

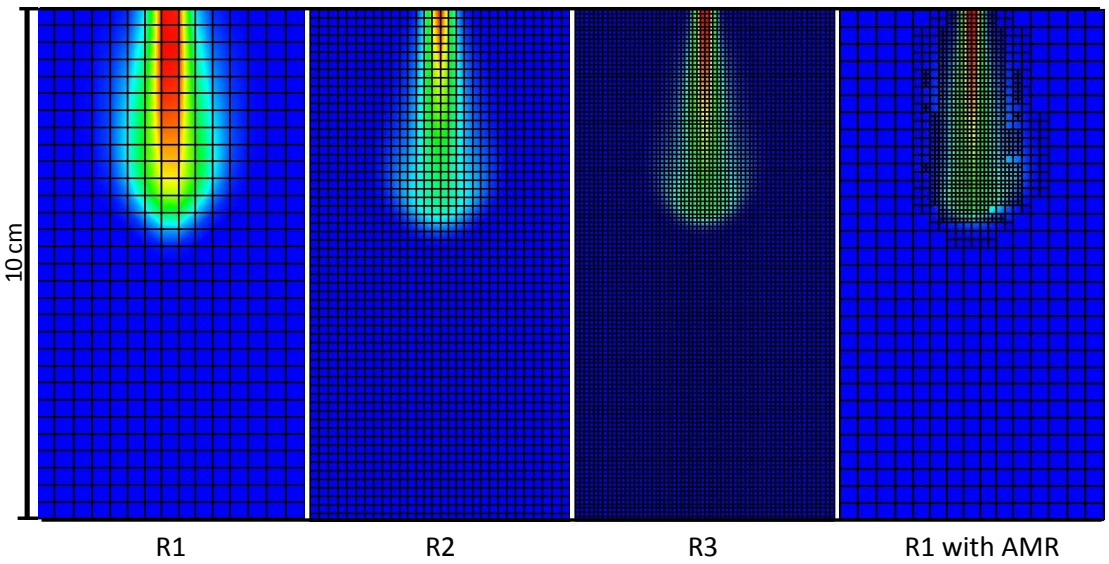

Figure 3.1 Hydrogen mass fraction contours in a constant volume chamber using R1, R2, R3 grids, and R1 grid with AMR at 1 ms after injection.

Additionally, the difference in the refinement level of adjacent cells is limited to one such that the AMR mesh will have smooth transitions. In addition, the refinement is deactivated on cells neighboring the moving boundaries in order to prevent numerical difficulties in the present code. It is noted that further improvement in the present AMR algorithm is needed in order to capture mixture formation more accurately near the moving walls [45]. Nonetheless, the present AMR is mainly used to capture the hydrogen jet near the injector when the velocity and hydrogen concentration are high. When a cell is refined, it is first divided into eight sub cells in the first level refinement. Each sub cell is then divided into eight second level sub cells in the second level refinement. The AMR algorithm is called at regular intervals during the solution cycles. In this study, an interval of 10 time steps is used for adaptation. This interval was determined based on numerical investigations considering computational time and solution accuracy. Once a group of child cells no longer satisfy the refinement criteria, they are coarsened to restore to their parent cell.

Figure 3.1 also shows the results using the R1 grid with AMR, and the predicted jet structure is similar to that using R3. It is worth noting that the computer time is 9.73 hours using the R1 grid with AMR. Thus, by using the proposed AMR algorithm it is possible to capture the hydrogen jet structure with reasonable computer time.

CHAPTER 4 MODEL VALIDATION

Validations on the hydrogen jet model developed in this study will be discussed in this chapter. The simulation results are validated against available experimental data. The jet penetration is chosen as the quantity to be compared, including single jet penetration and multiple jet penetrations. Johnson et al. [35] measured hydrogen penetration for single jet injection. Although the measured penetration data were obtained under combustion conditions, it was observed from previous experiments using methane injection that there is only a slight difference between penetrations with and without combustion. The multiple jet experiments were conducted by Peterson et al. [15], and the jet penetrations were measured using Schlieren visualization technique.

3.1 Single Jet Validation

The model was applied to simulate the experiments of hydrogen injection [35]. Hydrogen is injected at a pressure of 207 bar and temperature of 450 K to a constant volume chamber of air with pressure 62 bar and temperature 1150 K. The nozzle diameter is 250 μm. The computational domain used in the simulation consists of a constant volume cylindrical chamber with 10 cm in diameter and 20 cm in height. The domain is meshed using an O-grid scheme with the circular facing assumed as a logical square. The domain is divided into 30x30x60 cells. For an average cell size of 3.33 mm, the inflow boundary location is Z_{in} = 7.24 mm. This mesh is used together with AMR with two-level refinement. The jet tip penetration is measured as the penetration of 3% mass fraction of hydrogen. The predicted

penetration is compared with the measured experimental penetration, as shown in Figure 4.1. Results show that the jet penetrates at a higher rate initially. As the jet expands, the tip penetration gradually slows down. The model predicts the same trend and magnitude as in the experimental data. Overall, good agreement between simulation and experiment is obtained. Despite that the predicted penetration is slightly longer than the experimental data. The results are within 5% accuracy.

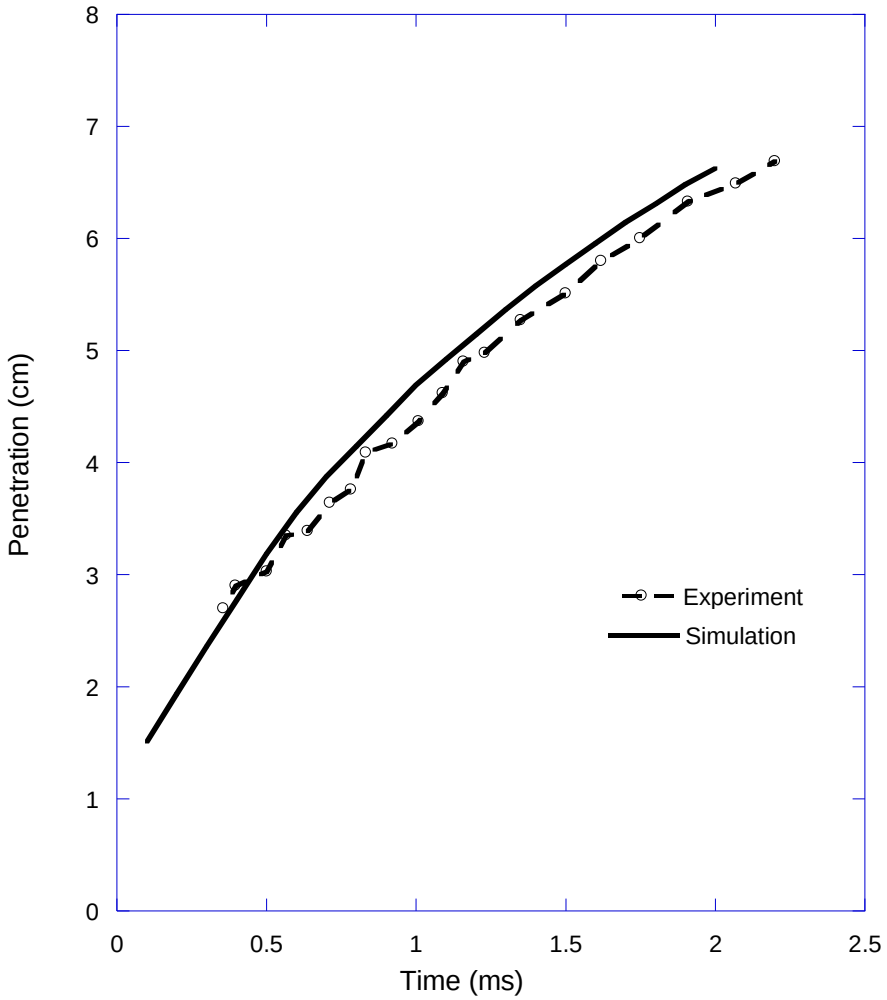

Figure 4.1 Comparisons of experimental and numerical results of the hydrogen jet penetration.

The present model was also used to simulate helium injection. In this validation case, as there are no experimental data available for validation, the jet penetration obtained using a theoretical correlation is used for model validation. The theoretical equation for the jet penetration [30] can be written as a function of time as Eq. (4.1)

$$Z = \sqrt{\left(2k_d U_n d_n (\rho_g/\rho_{ch})^{1/2} t\right)} \tag{4.1}$$

The variables have the same meaning as mentioned in Section 2.2. The nozzle diameter is 127 μm. The injection pressure and temperature are 6.73 bar and 296 K, respectively, and the pressure and temperature of air in the chamber are 1.013 bar and 296 K, respectively. The simulation was conducted on a cylindrical domain of 10 cm in diameter and 10 cm in height, descretized into 30x30x30 cells. The Mach disk diameter and the sonic velocity at the Mach disk were calculated to be 0.23 mm and 875 m/s, respectively. The predicted jet penetration is compared with the theoretical results, as shown in Figure 4.2. Good levels of agreement are obtained by using the present model with AMR.

Note that from the empirical correlations of Ewan and Moodie [24], the length of the barrel shock from the injector nozzle in the above two cases is 227 μm and 123 μm, respectively. Thus, the distance from the nozzle exit to the Mach disk can be neglected in the calculation of jet penetration. The above results indicate that using the present gas injection model with AMR, underexpanded gas jets can be predicted with a reasonable accuracy on a coarse mesh.

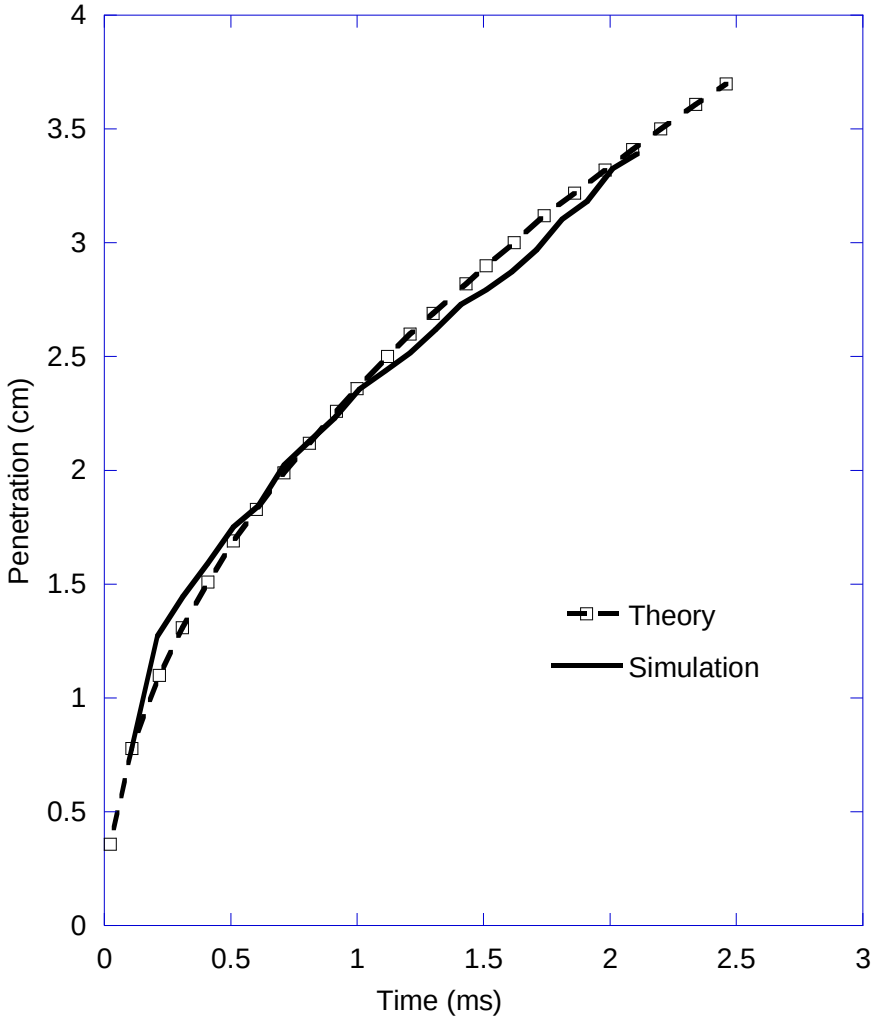

Figure 4.2 Comparisons of theoretical and numerical penetrations of a helium jet.

3.2 Multiple Jets Validation

The hydrogen jet penetration using a multiple-nozzle injector was measured using the Schlieren visualization technique [15]. Two cases were selected to validate the present model in simulating multiple jet injection. In the first case, hydrogen is injected using a three-nozzle injector at a pressure of 104 bar into a chamber with nitrogen at 3.36 bar. The temperature is kept at 298 K at the injector and in the chamber. The nozzle diameter is 0.8 mm. The numerical simulation was performed on a cylindrical geometry with 20 cm in diameter and 10 cm in height, descretized

into 60x60x30 cells. Figure 4.3 shows the contours of hydrogen mass fraction and the iso-surface of 0.3% hydrogen mass fraction compared with the experimental images. Results show good agreement between the numerical and experiment data, as shown in Figure 4.4.

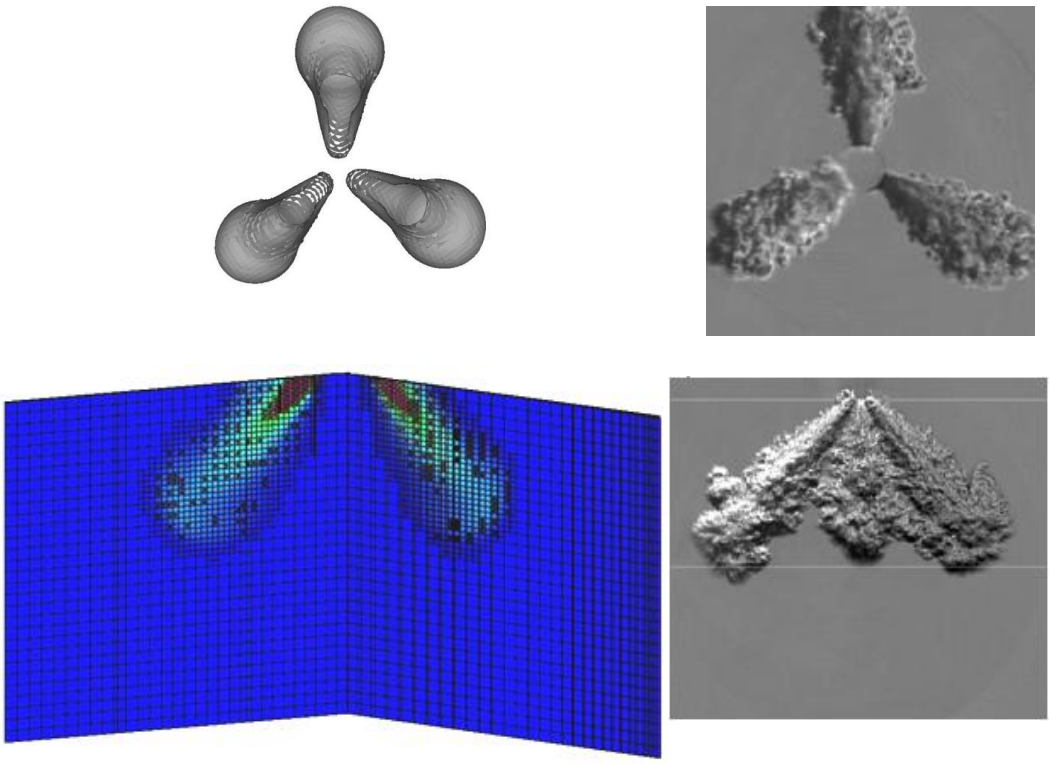

(a) (b)

Figure 4.3 (a) Predicted iso-surface of 0.3% hydrogen mass fraction (top) and contours of hydrogen along the injection planes (bottom).
(b) Top view and side view of the experimental Schlieren images [15].

In the second case, the chamber pressure is increased to 7.2 bar. The rest of the parameters are kept the same. The simulation results and experimental data are also compared in Figure 4.4. The present gas jet model with AMR is able to

accurately predict the injection of multiple jets using a coarse mesh. It can also be inferred from the results that as the pressure inside the chamber increases, the penetration length decreases.

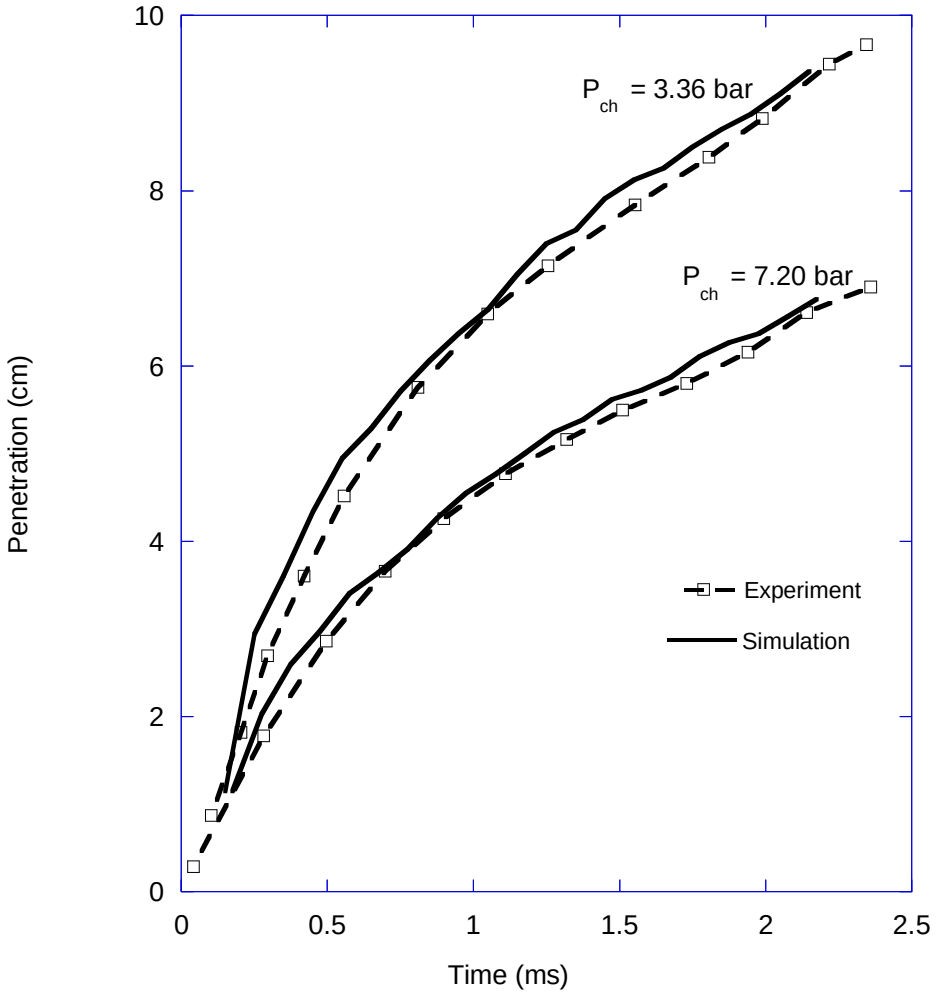

Figure 4.4 Comparisons of experimental and numerical hydrogen penetrations for the multiple jet injection.

CHAPTER 5 MIXTURE FORMATION IN IC ENGINES

The objective of this work is to study the hydrogen mixture formation in IC engines. As described in the previous chapters, a hydrogen jet model is implemented in the multidimensional CFD code, KIVA-4, and the model is validated using the experimental data. In this chapter, the model is further applied to in-cylinder hydrogen injection and the transient engine cycle is simulated. The injection parameters are varied and a parametric study is performed to determine the effects of injection parameters on the mixture formation inside the engine.

5.1 In-Cylinder Mixture Formation

The model was applied to simulate the in-cylinder mixture formation of a two-valve, direct-injection spark-ignition engine. The details of the engine are listed in Table 5.1. The parameters to be studied include the injection timing, the injector location, and the included angle of injection (i.e., orientation of nozzle). In this study, the quality of the air-fuel mixture is evaluated based on the equivalence ratio distribution in the engine cylinder. Although it is ideal to create a stratified mixture around the spark plug [6] it may be difficult to have quantitative criteria to describe the stratification. Therefore, in the present study, mixture homogeneity was chosen as the criterion to assess the injection parameters since basically an SI engine requires a homogeneous mixture. Particularly, under direct-injection conditions, there is limited time for mixture preparation. Thus, mixture homogeneity appears to be an appropriate criterion.

Table 5.1 Engine specifications

Number of Valves	2
Piston type	Flat Piston
Bore (cm)	14
Stroke (cm)	17.5
Squish (cm)	2.5
Intake Valve Timing	IVO = 20 BTDC, IVC = 215 ATDC
Exhaust Valve Timing	EVO = 495 ATDC, EVC = 10 ATDC
Speed (RPM)	1000
Injector	3-hole injector
Compression Ratio	8:1

Hydrogen is injected at a pressure of 413 bar and temperature of 298 K. The pressure inside the engine is used as the chamber pressure in the gas injection model, e.g. Eq. (3). The injector has three nozzle holes and each nozzle has a diameter of 200 µm. The computational mesh is shown in Figure 5.1. The mesh consists of approximately 30,000 cells at the bottom-dead-center (BDC). The simulation starts from 20 degrees before top-dead-center (BTDC) and ends at 360 degrees after top-dead-center (ATDC), which is an appropriate timing to assess the mixture homogeneity. In the present engine, the intake valve opens at 20 BTDC and the exhaust valve closes at 10 ATDC. Thus, the simulation includes the entire intake process together with part of the exhaust process. This study is focused on the mixture formation before combustion occurs. Because combustion is not modeled, the simulation of the entire exhaust process may not be of significance since the exhaust of combustion products and the mixing of residuals and fresh air are not

considered. Hydrogen is injected after both valves are closed to prevent the leakage of fuel through the valve opening. The mass of hydrogen injected corresponds to an overall equivalence ratio (ER) of 0.45. The effect of natural convection can be neglected as the ration Gr/Re^2 was found to be of the order of 1.0e-5.

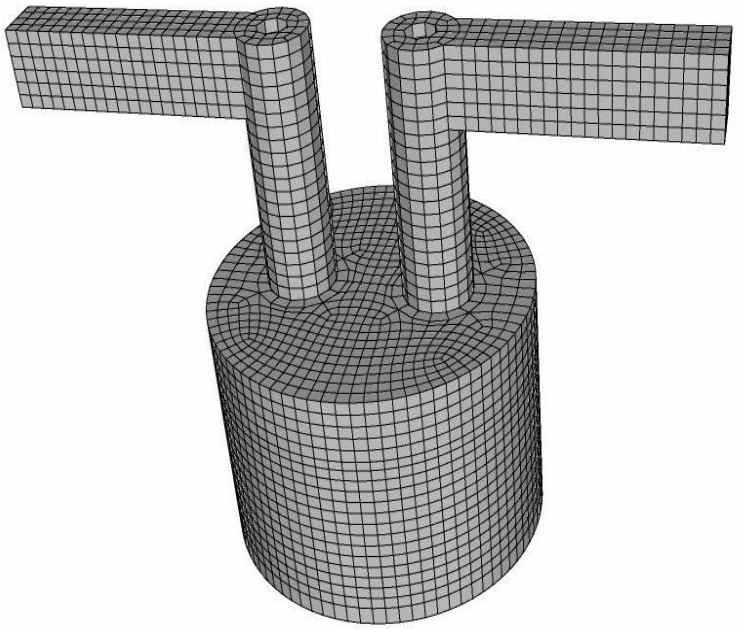

Figure 5.1 Computational grid of the engine used for parametric study

The start of injection (SOI) timings used for the present parametric study are 220, 240, and 260 ATDC. Three injector locations are studied, including one near the intake valve, one near the exhaust valve, and one in between the valves. At each of these locations, three different included angles of injection are tested, including 30, 45, and 60 degrees as shown in Figure 5.2. The above conditions are listed in Table 5.2 and the schematic of the injector locations are also shown in Figure 5.2. These

conditions are chosen based on the experimental conditions in a previous study [13]. The average run time of the entire simulation is 28 hours on a single processor.

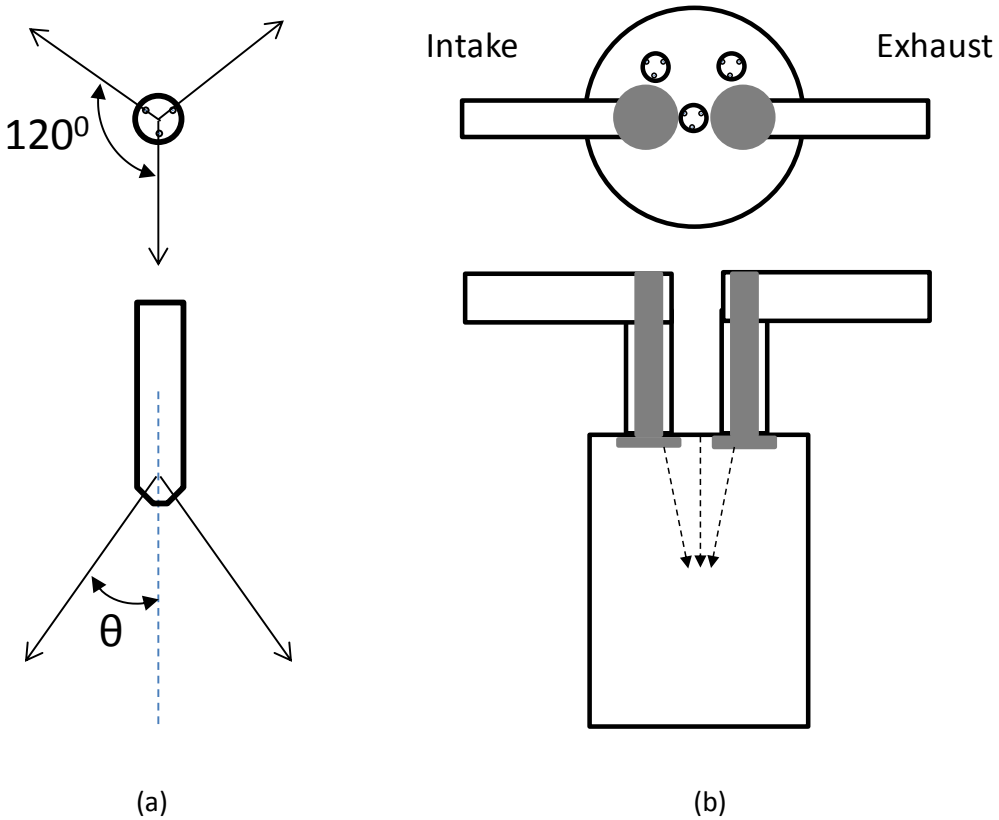

(a) (b)

Figure 5.2 (a) Top view and side view of the injection angle. Three different included angles are studied, $\theta = 30^0, 45^0, 60^0$.
(b)Three different injector locations and the corresponding orientation of the injector axis at each location.

The in-cylinder flow field prior to and during hydrogen injection for Case 1 is shown in Figure 5.3. The flow field prior to injection will be same for all the cases where the start of injection is maintained the same, as only the injection parameters are different in each case. The hydrogen jet has a relatively high velocity entering the combustion chamber. Note that a gas injection model is used in this study to prevent the modeling of the supersonic jet. Thus, the entrance velocity to the computational

domain is subsonic and is diffused rapidly. Nonetheless, the disturbance to the flow field due to the high gas jet velocity can be observed from these images.

Table 5.2 Conditions and results of the parametric study cases

Case	Included angle of injection (degrees)	SOI (ATDC)	Injector location	Equivalence ratio range at 360ATDC	Cylinder volume fraction for equivalence ratio from 0.4 to 0.5
Case 1	45	220	Between valves	0.20-0.60	28%
Case 2	45	240	Between valves	0.15-0.90	20%
Case 3	45	260	Between valves	0.15-0.90	15%
Case 4	30	220	Between valves	0.15-0.75	20%
Case 5	60	220	Between valves	0.10-0.75	22%
Case 6	30	220	Near intake	0.25-0.65	30%
Case 7	45	220	Near intake	0.25-0.65	36%
Case 8	60	220	Near intake	0.25-0.62	50%
Case 9	30	220	Near exhaust	0.20-0.62	41%
Case 10	45	220	Near exhaust	0.15-0.75	30%
Case 11	60	220	Near exhaust	0.25-0.75	30%

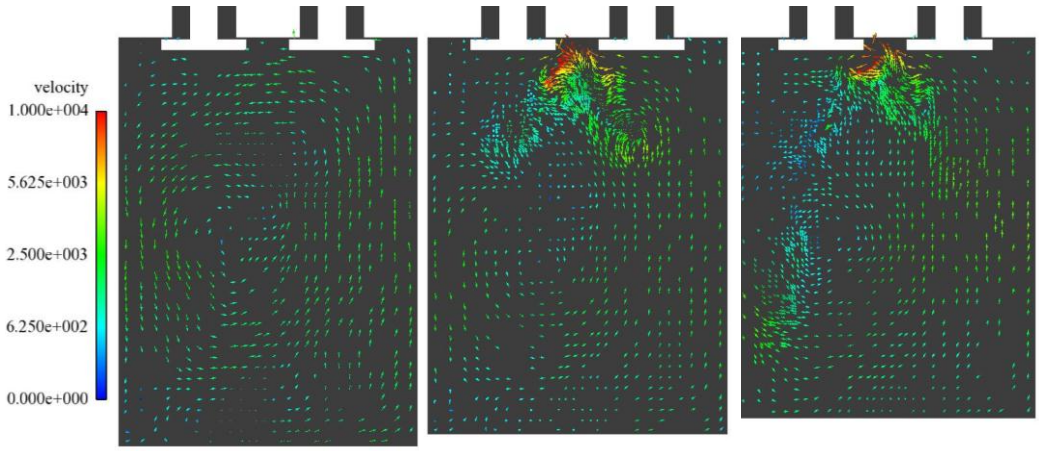

215 ATDC 225 ATDC 235 ATDC

Figure 5.3 Flow field prior to and during hydrogen injection. Velocity vectors are colored by the velocity magnitude (cm/s).

5.2 Qualitative Analysis of Mixture Formation

A qualitative evaluation of each case can be obtained by assessing the hydrogen mass fraction contours at different times. The solution is visualized using EnSight visualization software. The solution variables from KIVA-4 are exported in EnSight format at regular intervals. The hydrogen mass fraction contours are visualized on different cut planes to analyze the propagation of the fuel from the injector to the engine cylinder. The regions of high fuel content and low fuel content can be identified through the mass fraction contours. In the following sections the mixture formation in each case is analyzed qualitatively using hydrogen mass fraction contours.

5.2.1 Case 1

The detailed mixture formation process for Case 1 with center injection is shown in Figure 5.4. The included angle of injection is 45 degrees. The mixing process can be seen from the evolution of the contour of hydrogen mass fraction. Note that these images are plotted on the cut planes aligned with the two gas jet directions, i.e., 120 degrees included angle. The interactions of fuel jets with walls and the in-cylinder flow can be seen from these images. Two fuel jets evolve differently as the cycle progresses because the intake and exhaust valves are located at different sides. After wall impingement, one of the fuel jets moves along the cylinder wall towards the piston. The other jet spreads transverse to the cut plane and towards the cylinder head along the cylinder walls. This difference can be explained using the in-cylinder flow field. The air intake through the intake valves

and the motion of the piston creates swirl and tumble inside the cylinder. The swirl creates circulating currents perpendicular to the piston surface and the tumble creates circulating currents perpendicular to swirl. The tumble inside the engine can be observed in Figure 5.3. The difference in evolution of the fuel jets is due to the effects of this swirl and tumble inside the cylinder. Overall, the final mixture distribution is determined by the interactions of the fuel jet, cylinder walls, and in-cylinder flows.

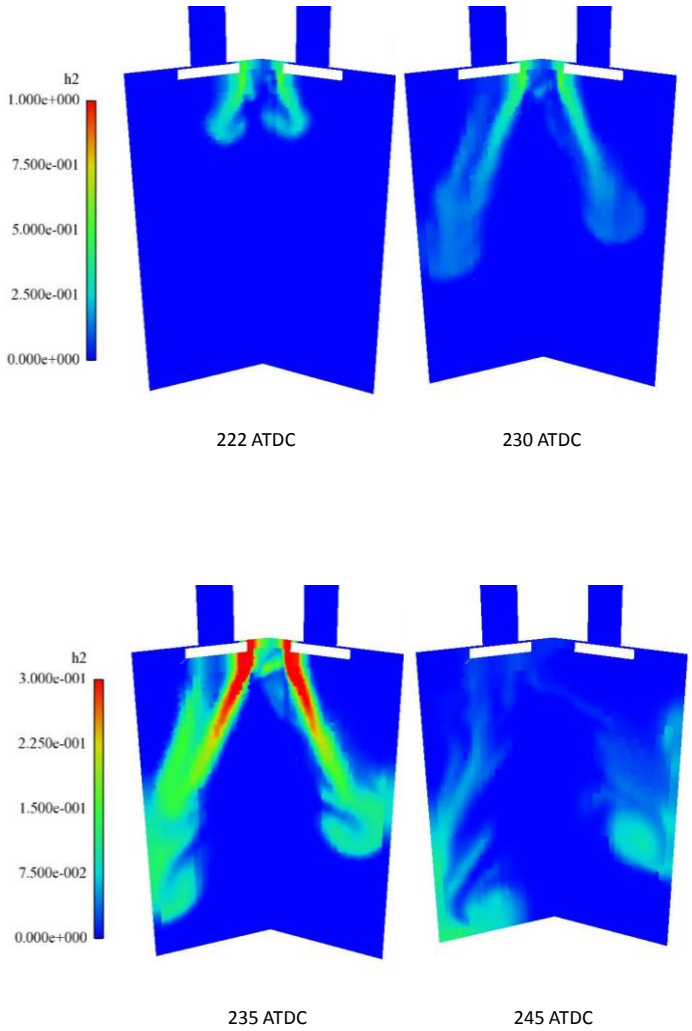

Figure 5.4 Hydrogen mass fraction on the injection planes at different times for Case 1.

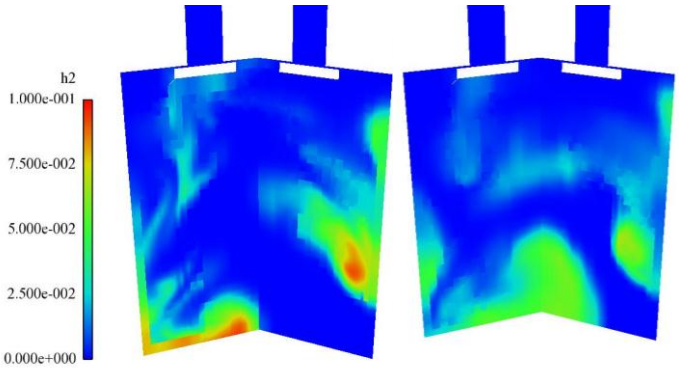

250 ATDC 260 ATDC

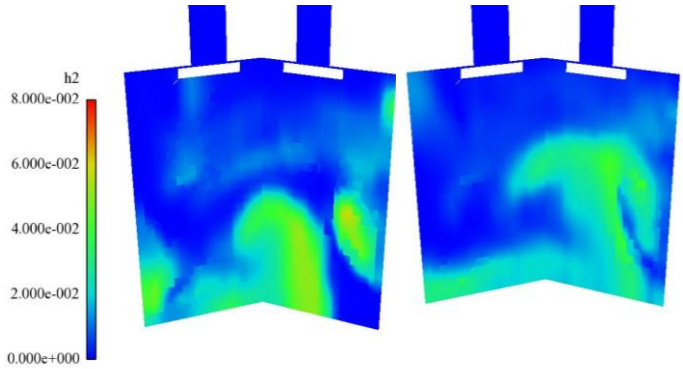

265 ATDC 275 ATDC

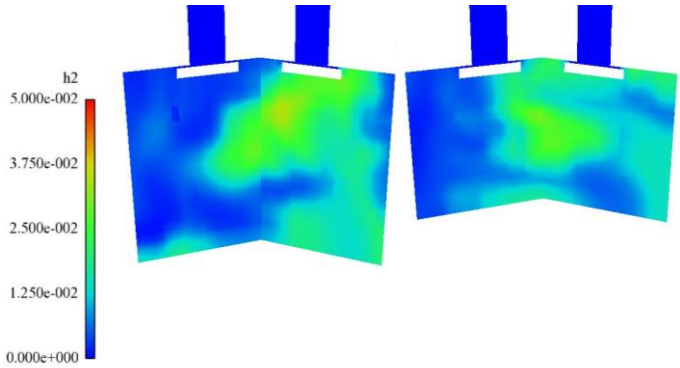

290 ATDC 305 ATDC

Figure 5.4 (Continued).

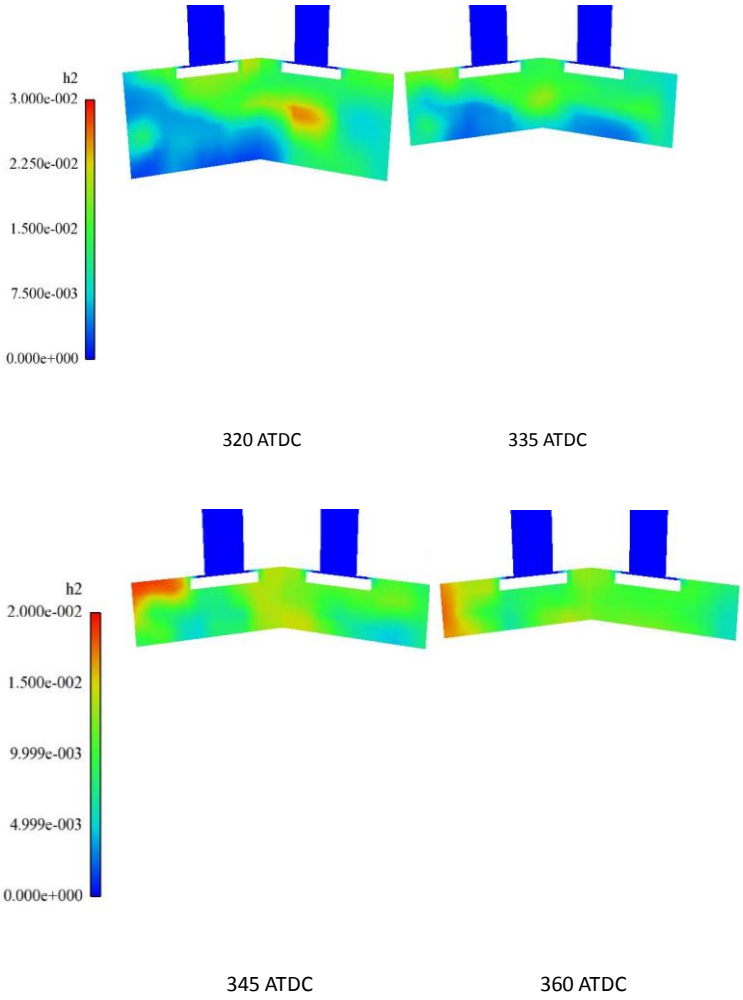

Figure 5.4 (Continued).

The detailed mixture formation process of the rest of the cases is not shown. However the hydrogen mass fraction contour during the injection and at 360 ATDC is shown for each case below. The contours are plotted on vertical and horizontal planes in order to visualize the fuel distribution inside the cylinder. Two injection planes are selected as the vertical planes, for Case 2 and Case 3, where the SOI is varied. From Case 4 to Case 11, where the injection location and included angle of injection are varied, the geometric symmetry plane is selected as the vertical plane.

The horizontal plane is selected as a plane 0.5 cm below the cylinder head. The valve regions can be seen in this plane.

5.2.2 Case 2

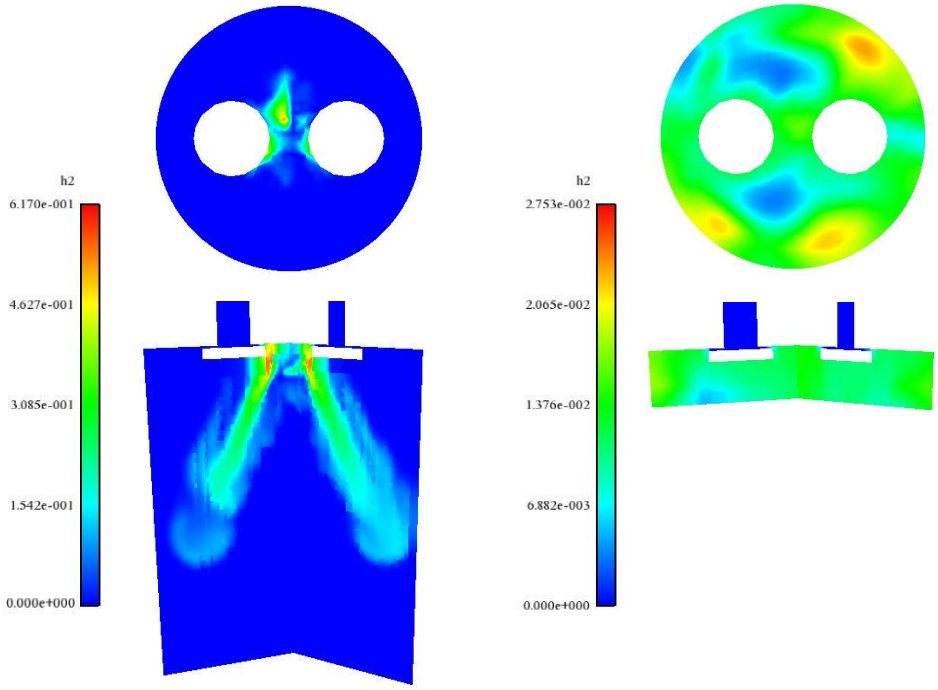

Figure 5.5 Hydrogen mass fraction on the injection planes during injection and at 360 ATDC for Case 2

The hydrogen mass fraction contours at 250 ATDC and 360 ATDC of Case 2 along the injection planes and at a horizontal plane 0.5 cm below the cylinder head are shown in Figure 5.5. In this case, the three fuel jets are oriented at 120 degrees apart and at an angle of 45 degrees from vertical. In Figure 5.5, the top view of the mass fraction contours clearly shows the injection locations of the three hydrogen jets. From the side view of fuel mass fraction contours, the angle of fuel jets can be seen. It can be observed that the hydrogen jets hit the cylinder wall. The mixture

formation process is similar to the case 1. However, the residence time of the fuel inside the cylinder is less and hence the final mixture in this case has regions of high and low fuel concentration. The pockets of fuel rich regions were found inside the cylinder close to the cylinder head. The boundaries of these pockets are visible in the top view at 360 ATDC. There are regions of low fuel content near the cylinder head, which can be seen in the contour image shown and also near the piston surface, a portion of which is visible in the vertical plane at 360 ATDC. The highest fuel mass fraction in the cylinder can be determined from the maximum value of the hydrogen mass fraction contour legend. In this case, the highest mass fraction was found close to the cylinder head and has a value of 0.0275. The corresponding equivalence ratio can be calculated as 0.98. The ideal homogeneous mixture should have a mass fraction of 0.0128 which corresponds to the overall equivalence ratio of 0.45 homogeneous mixture should have a mass fraction of 0.0128 which corresponds to the overall equivalence ratio of 0.45

5.2.3 Case 3

The initial and final hydrogen mass fraction contours on two injection planes for Case 3 are shown in Figure 5.6. The start of injection is at 260 ATDC. The piston is under compression stroke at this crank angle and has completed nearly half of the stroke length. As a result, the chamber pressure during injection is higher than the previous cases. This resulted in a slower penetration of the jet. However, the upward motion of the piston makes the jet to impinge on the piston surface at 270 ATDC. It was also observed that the included angle of fuel jets was reduced as the jet progress through the in-cylinder. Although the injection angle if 45 degrees, the fuel

jets do not spread as observed in the previous cases. After impinging the piston surface, the fuel spreads along the piston towards the cylinder wall. The fuel then moves along the cylinder wall upwards. The final mixture contains very rich and lean regions. The fuel rich region, which is not visible in Figure 5.6, was observed near the exhaust valve and near the piston surface closer to the cylinder walls. There are regions with fuel mass fraction as high as 0.03512 near the piston surface. Also there are regions inside the cylinder with virtually no fuel present which can be noticed in Figure 5.6.

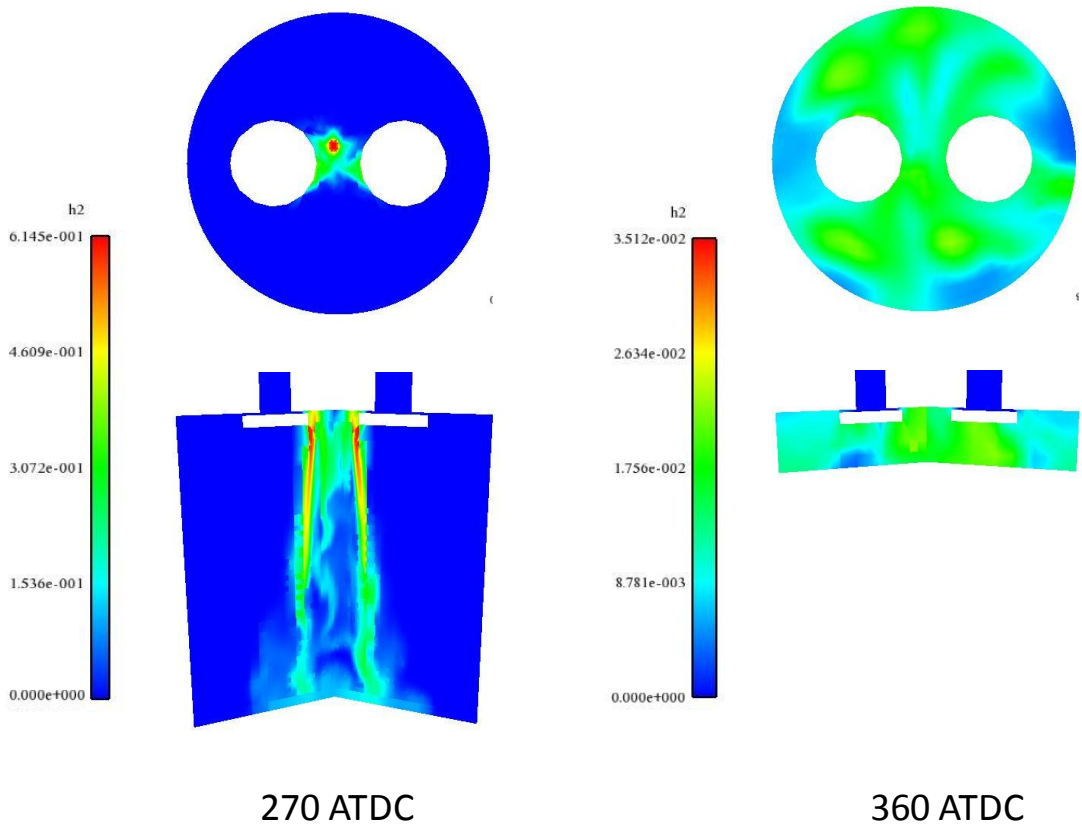

Figure 5.6 Hydrogen mass fraction contours on a horizontal plane 0.5 cm below the cylinder head and the injection planes for Case 3

5.2.4 Case 4

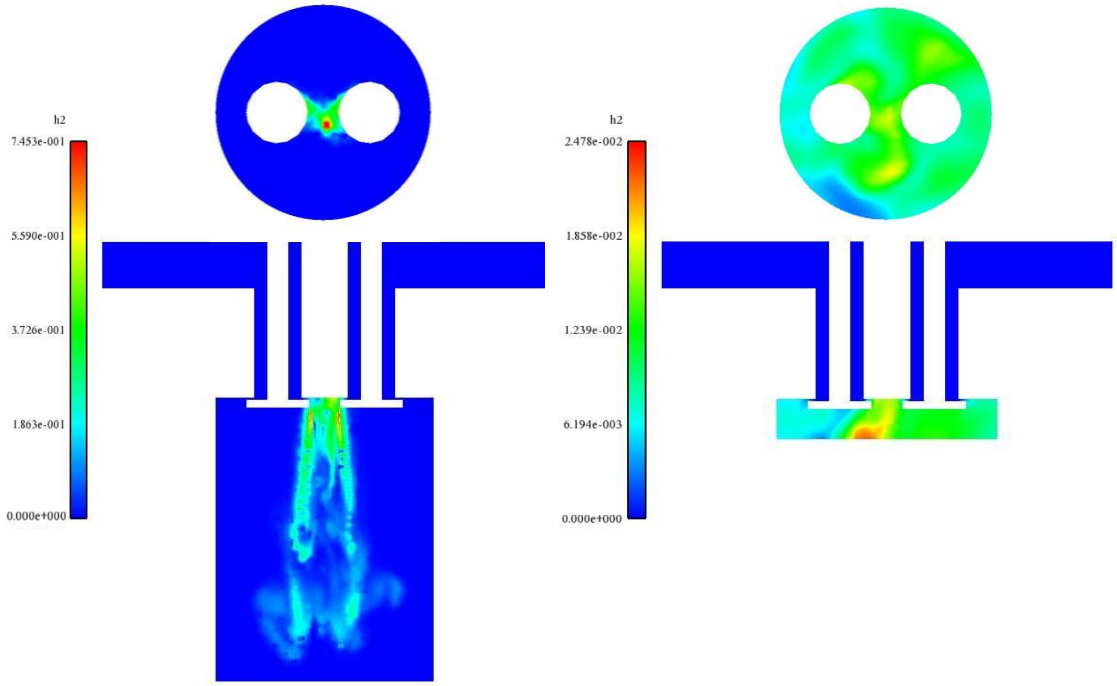

Figure 5.7 Hydrogen mass fraction contours on a horizontal plane 0.5 cm below the cylinder head and at the vertical symmetric plane for Case 4

Figure 5.7 is the side view and top view of Case 4 at 230 ATDC and 360 ATDC. Hydrogen is injected at 220 ATDC at an included angle of 30 degrees. The fuel jets impinge on the piston surface. After impingement, the fuel spreads along the piston surface towards the cylinder wall. As the cycle progresses, the fuel crawls up along the cylinder wall. It can be seen from the contours at 360 ATDC that there are regions inside the cylinder with high fuel content near the piston surface and some regions of low fuel content near by the cylinder wall.

5.2.5 Case 5

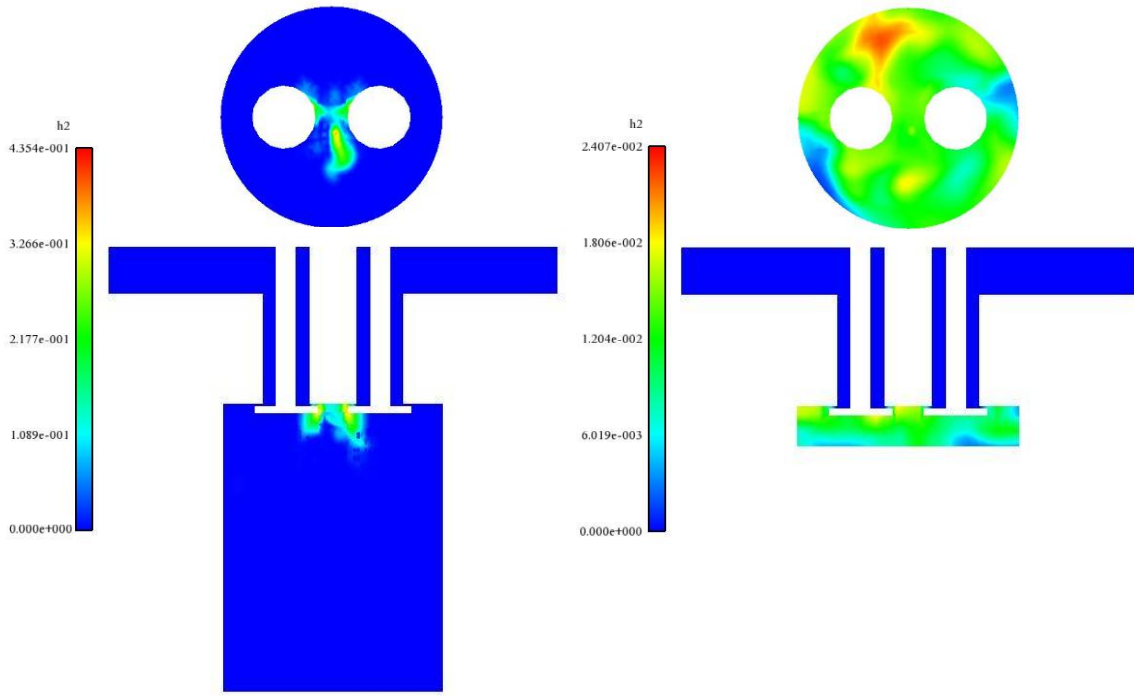

Figure 5.8 Hydrogen mass fraction contours on a horizontal plane 0.5 cm below the cylinder head and at the vertical symmetric plane for Case 5

The initial and final hydrogen mass fraction contours for Case 5 are shown in Figure 5.8. The fuel jet is injected at an angle of 60 degrees. As a result the entire fuel penetration is not visible in the vertical plane. It was observed that the fuel jets hit the cylinder wall at 232 ATDC. The fuel jets then moves along the cylinder walls towards piston. In the final mixture, a fuel rich region was found near the cylinder head which can be observed in the top view at 360 ATDC. Lean regions were found near the cylinder head and piston surface.

5.2.6 Case 6

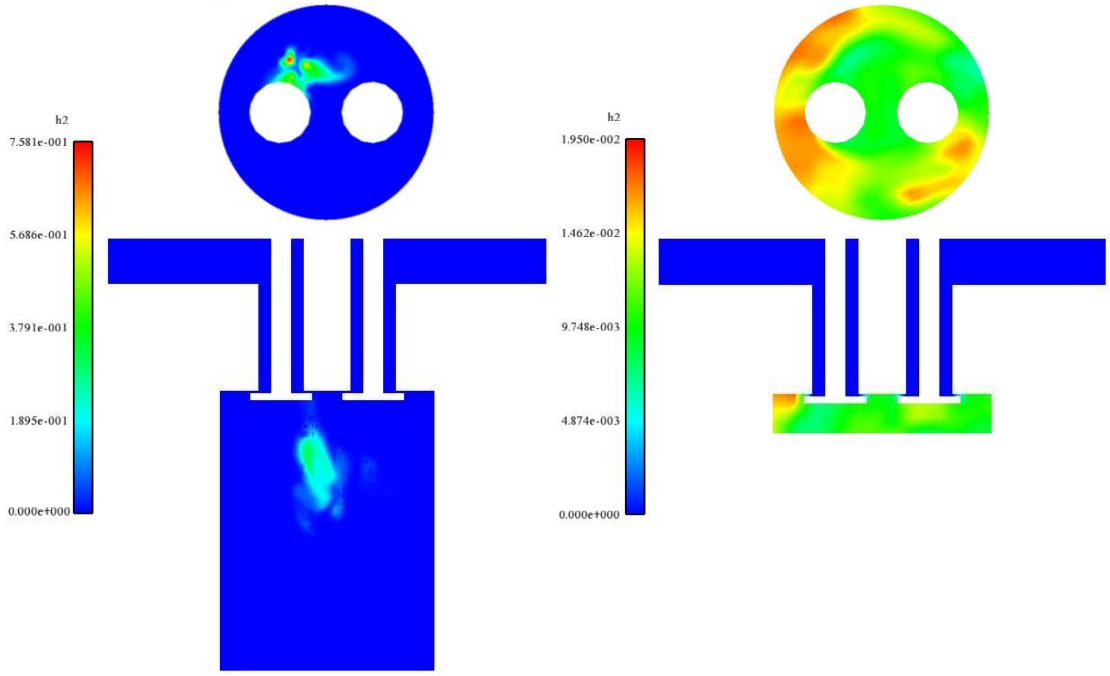

Figure 5.9 Hydrogen mass fraction contours on a horizontal plane 0.5 cm below the cylinder head and at the vertical symmetric plane for Case 6

Hydrogen mass fraction contours for the case 6 are shown in Figure 5.9. The injector location is near the intake valve and the included angle of injection is 30 degrees. The three inlet boundaries used for injection can be seen in the top view at 230 ATDC. A section of one of the fuel jet can be seen in the vertical plane at 230 ATDC. The fuel jets hits the cylinder wall at different times. The last fuel jet impingement occurs at 245 ATDC. After wall impingement, two of the fuel streams crawl down towards the piston. The third one spreads along the cylinder wall. The final mixture has fuel rich regions nearby the cylinder wall at the intake valve side. There was no region of very low fuel content.

5.2.7 Case 7

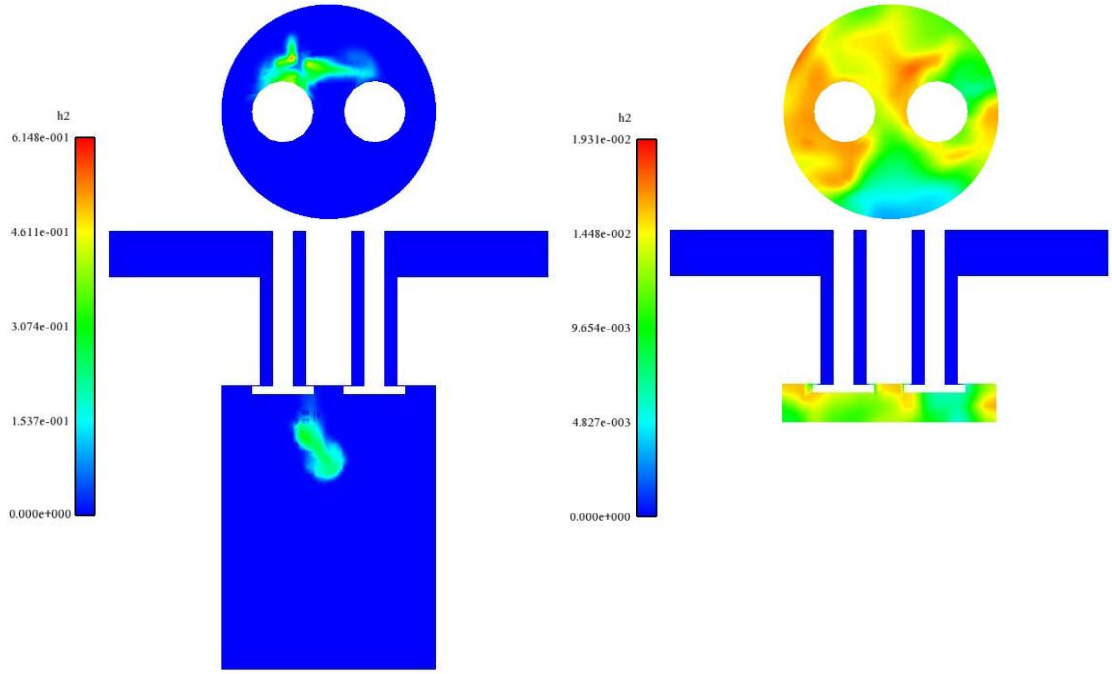

Figure 5.10 Hydrogen mass fraction contours on a horizontal plane 0.5 cm below the cylinder head and at the vertical symmetric plane for Case 7

Figure 5.10 shows the hydrogen mass fraction contours of Case 7. The injector location is near the intake valve and included angle of injection is 45 degrees. Similar to the previous case, the fuel jets hits the cylinder wall at different times. However the locations of jet impingements are different. The last fuel jet impingement occurs at 250 ATDC. Two of the fuel streams crawl down along the cylinder wall towards the piston. The third one spread along the cylinder wall. The final mixture has fuel rich regions nearby both the valves. There was a region of low fuel content near the cylinder wall, away from the injection side.

5.2.8 Case 8

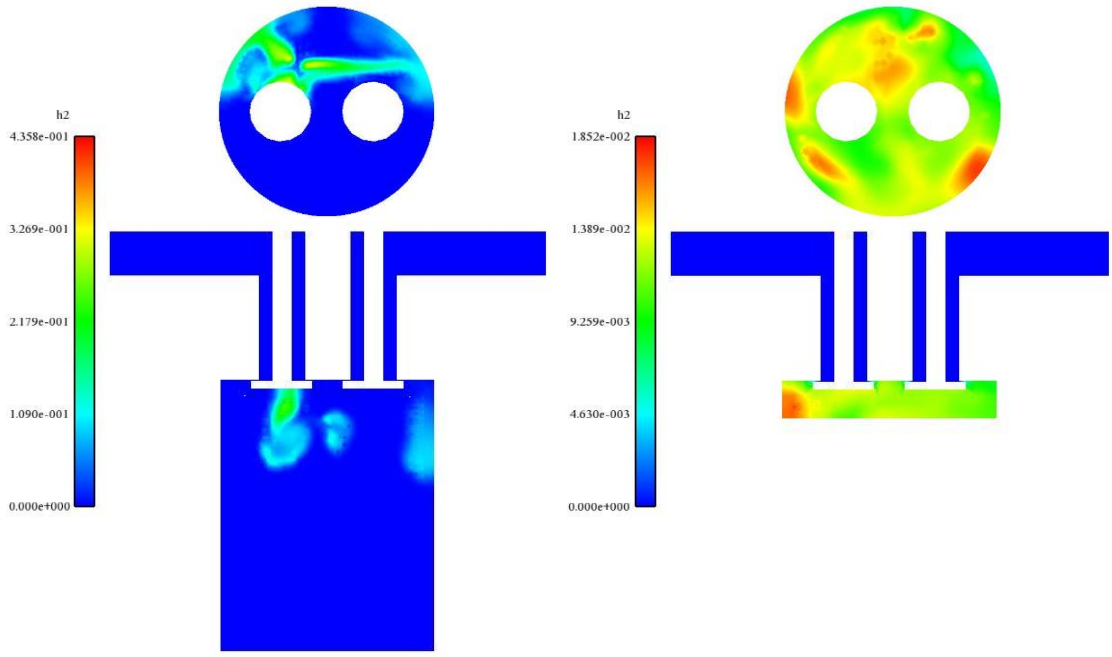

Figure 5.11 Hydrogen mass fraction contours on a horizontal plane 0.5 cm below the cylinder head and at the vertical symmetric plane for Case 8

Figure 5.11 is the side view and top view for Case 8 at 230 ATDC and 360 ATDC. The locations of the three nozzle holes can be easily recognized by the high local equivalence ratio in the figure. The injector is oriented towards the center of the cylinder. The three fuel jets are oriented at an angle of 60 degrees from the center line of injector. Hydrogen is injected at 220 ATDC. It is observed from the contours that, by 235 ATDC, the fuel jets have already impinged on the cylinder walls and have started mixing with the air. Small pockets of rich mixtures were observed near the intake valve and near the piston surface. There was no region of very low fuel content.

5.2.9 Case 9

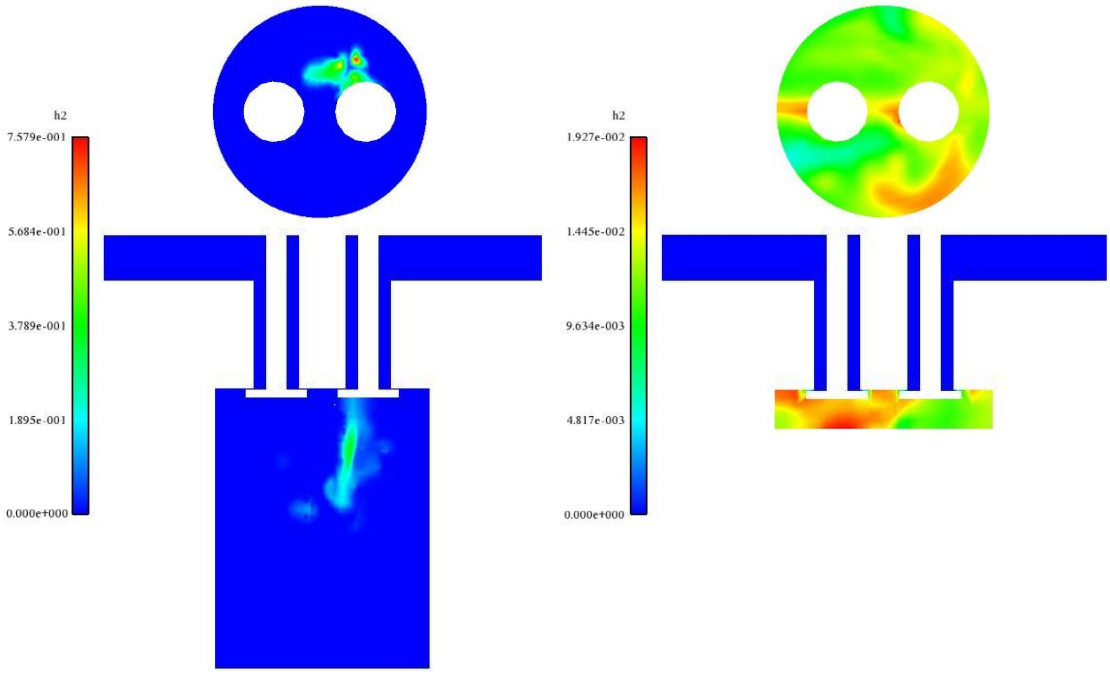

Figure 5.12 Hydrogen mass fraction contours on a horizontal plane 0.5 cm below the cylinder head and at the vertical symmetric plane for Case 9

Figure 5.12 shows the hydrogen mass fraction contours of Case 9. The injector location is near the exhaust valve and the injection boundaries can be observed from the top view at 230 ATDC. Included angle of injection is 30 degrees. By 240 ATDC all the fuel jets reaches the cylinder wall. After hitting the wall, one of the fuel streams crawls down along the cylinder wall towards the piston. The other two spread along the cylinder wall. It is observed from the mass fraction contour that the final mixture has a fuel rich region below the intake valve. There was no region of very low fuel content.

5.2.10 Case 10

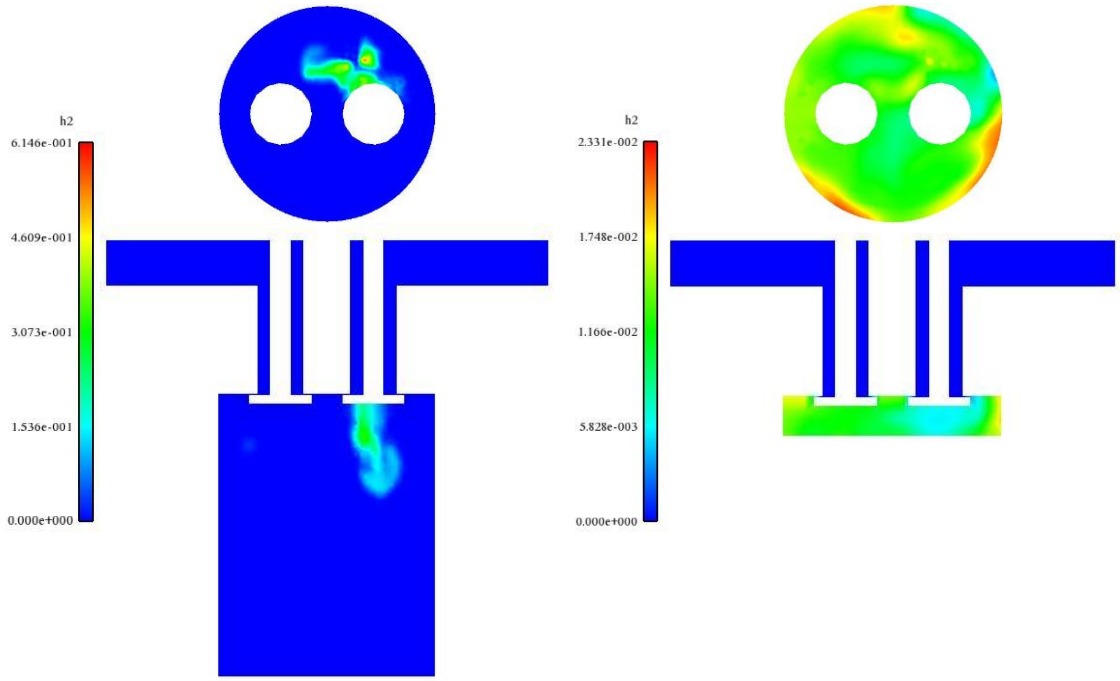

Figure 5.13 Hydrogen mass fraction contours on a horizontal plane 0.5 cm below the cylinder head and at the vertical symmetric plane for Case 10

Hydrogen mass fraction contours of Case 10 are shown in Figure 5.13. The included angle of injection is 45 degrees. The fuel jets hits the cylinder wall at different times. The last fuel jet impingement occurs at 232 ATDC. After wall impingement, two of the fuel streams move along the walls, towards the piston, while the third one spread along the cylinder wall. The final mixture has very rich regions nearby the cylinder wall, away from the injection side. It is noticeable that there are regions with hydrogen mass fraction as high as 0.0233. There are pockets of lean mixture regions below the exhaust valve and near the piston surface.

5.2.11 Case 11

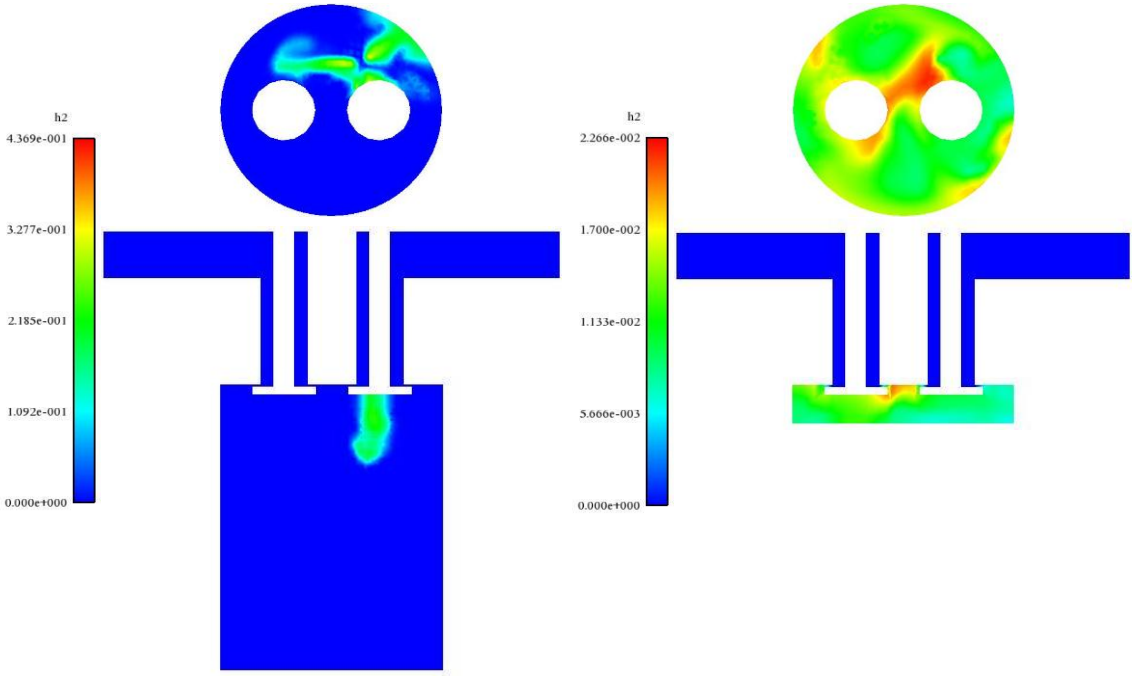

Figure 5.14 Hydrogen mass fraction contours on a horizontal plane 0.5 cm below the cylinder head and at the vertical symmetric plane for Case 11

Figure 5.14 shows the hydrogen mass fraction contours of Case 11. The included angle of injection is 60 degrees. Wall impingement of fuel jets occurs at about 232 ATDC. All the three jets hit the cylinder wall at the upper half. After that most of the fuel is spread along the cylinder walls. At 360 ATDC, very rich regions are found near the cylinder head close to intake valve and in between the valves. There was not any region with very low fuel content.

Based on the observation of the present simulation results, speaking overall, the hydrogen jets impinge on the cylinder wall or piston surface very quickly due to their high velocities. Before the wall impingement, the fuel-air mixing takes place

only in the narrow regions of fuel jets due to air entrainment. A majority of the fuel-air mixing occurs after wall impingement. Note that the present injection timing is relatively early, similar to those used in the previous experimental study [12]. As the injection timing is retarded, the in-cylinder density is higher, thus delaying the wall impingement. The effects of late injection needs to be further studied.

5.3 Quantitative Analysis of Mixture Distribution

The above equivalence ratio contours indicate the qualitative mixture distribution. In the following discussion, a quantitative measure is used for assessing the mixture distribution resulting from different injection conditions. During simulation, the equivalence ratio in each cell and the volume of the cell are exported from the computational results at regular time intervals. The cell volume is normalized by the total cylinder volume. The data of the computational cells are sorted in the ascending order of the equivalence ratio. Then, the normalized cell volumes below a specific equivalence ratio are added. As a result, the cumulative volume of the in-cylinder mixture below a specific equivalence ratio can be found. In other words, the percentage of the total volume in the cylinder that has equivalence ratios between two specific values can be obtained, i.e. the difference between the two cumulative volume fractions. Figure 5.15 shows examples of such equivalence ratio distribution curves at a specific crank angle. For instance Figure 5.15 (a) indicates that 49% of the total in-cylinder volume has an equivalence ratio lower than 0.2. Additionally, the mixture with an equivalence ratio between 0.2 and 0.5 occupies 22% of the cylinder (i.e., the difference of 0.49 and 0.71 cumulative volume). The figure also implies that 10% of the cylinder volume contains a rich

mixture with an equivalence ratio higher than 1.2. On the other hand, Figure 5.15 (b) shows an ideal case that has a homogeneous mixture of equivalence ratio 0.45. Therefore, if the purpose is to obtain a homogeneous mixture for premixed combustion, the goal will be to choose the injection conditions that can result in an equivalence ratio distribution curve as shown in Figure 5.15 (b). In the following discussion, the homogeneity of the in-cylinder mixture will be assessed based on the equivalence ratio distributions at different crank angle degrees.

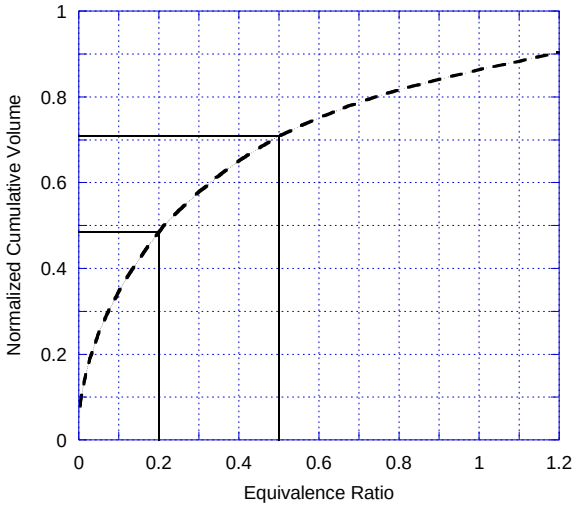

(a)

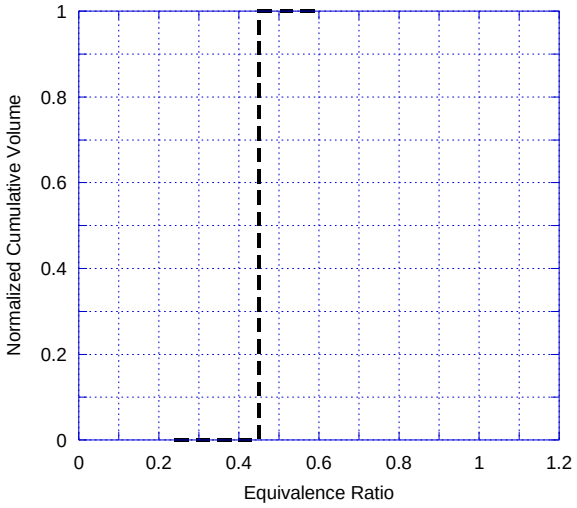

(b)

Figure 5.15 Examples of an equivalence ratio distribution curve
(a) 22% of the in-cylinder volume contains the mixture with an equivalence ratio from 0.2 to 0.5
(b) Ideal homogeneous mixture with an equivalence ratio of 0.45

Notice that the final assessment on the mixture homogeneity is based on the equivalence ratio distribution at 360 ATDC when the piston reaches top-dead-center. Despite that spark-ignition generally takes place before top-dead-center, flame propagation takes time and the combustion duration is usually 40 to 60 crank angle degrees. Thus, the overall combustion characteristics are closely related to the mixture distribution at top-dead-center since combustion is not modeled in this study.

5.3.1 Mixture Formation Characteristics with Different SOI

The engine is in the compression stroke when the fuel is injected. As the SOI is delayed, the volume of air to which the fuel is injected reduces and the residence time of fuel before the start of combustion decreases. A parametric study was conducted to analyze the dependence of fuel-air mixing on the SOI, i.e., Cases 1 to 3 in Table 5.2. The included angle of injection is fixed to 45 degrees and the injector is located between the valves as shown in Figure 5.5. The equivalence ratio distribution curves are plotted in Figure 5.16. For each case the equivalence ratio distribution at different times are shown. It is seen that the mixing is better for the early SOI case. The injected fuel has less time to mix with air in the cylinder as the SOI is retarded. As can be seen in Figure 5.16 (a) for Case 1 (SOI = 220 ATDC), the equivalence ratio ranges from 0.20 to 0.60 at 360 ATDC, compared to 0.15 to 0.90 for the other two cases. Note that the overall equivalence ratio is 0.45. For comparison, the percentage of volume with the equivalence ratio between 0.4 and 0.5 is approximately 28%, 20%, and 15% for Case 1, Case 2, and Case 3, respectively. Thus, 220 ATDC is used as the SOI for the rest of the remaining parametric study. It is also

observed that the fuel jet impinges on the side wall when the SOI is 220 ATDC and 240 ATDC, whereas it impinges on the piston when injected at 260 ATDC.

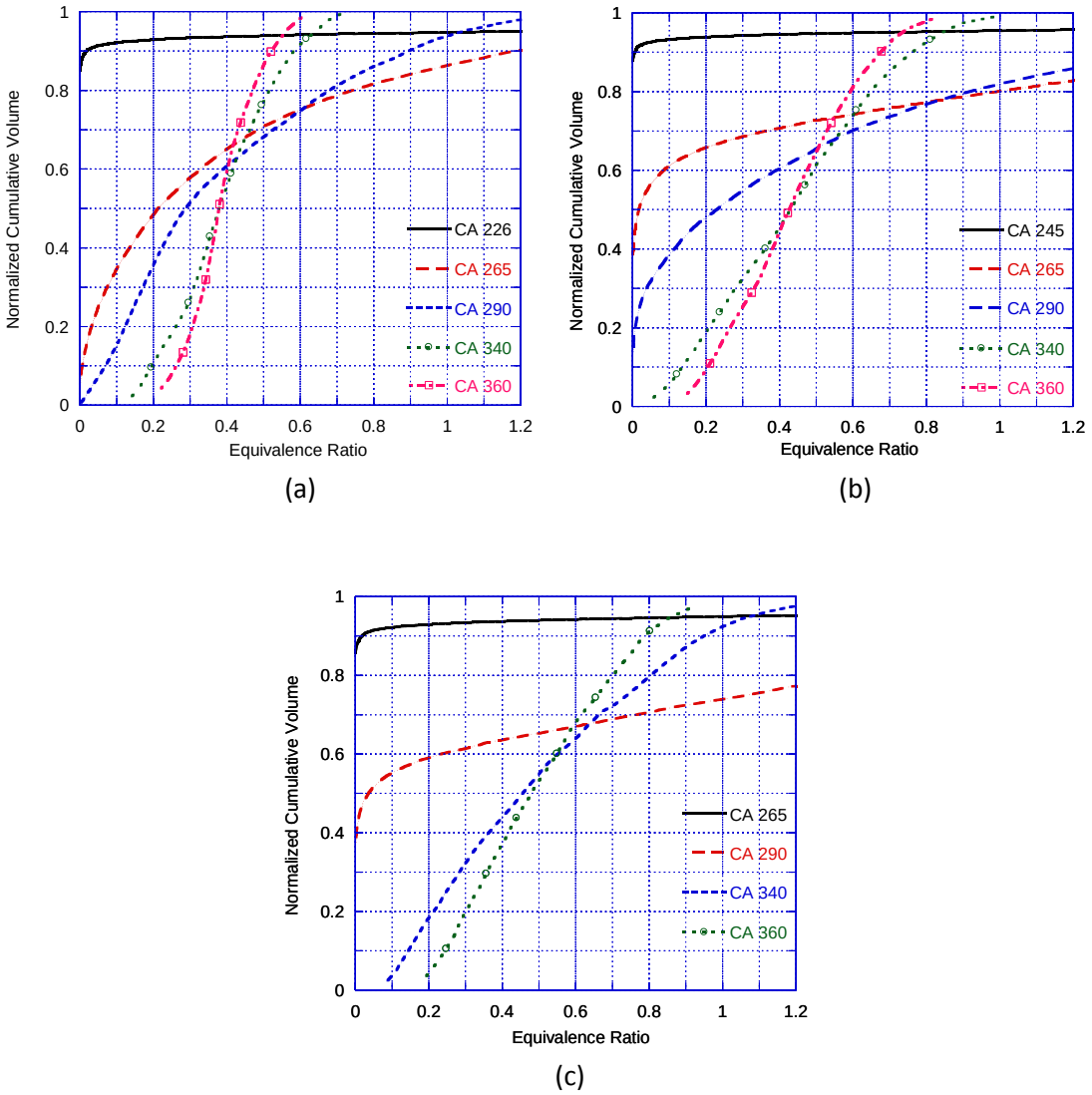

Figure 5.16 Equivalence ratio distributions at different crank angles for cases with 45 degrees injection angle and variable SOI
(a) Case 1: SOI = 220 ATDC (b) Case 2: SOI = 240 ATDC (c) Case 3: SOI = 260 ATDC

5.3.2 Mixture Formation Characteristics with Different Injection Angles and Injector Locations

The orientation of the fuel jets and the location of the fuel injector will have a prominent effect on the fuel-air mixing as the interactions of the fuel jets with the

cylinder walls and piston vary in each case. In this parametric study three injector locations are tested. At each injector location, the included angle of injection is varied as 30, 45, and 60 degrees from the centerline of the injector. For all the cases SOI is fixed at 220 ATDC, as listed in Table 5.2.

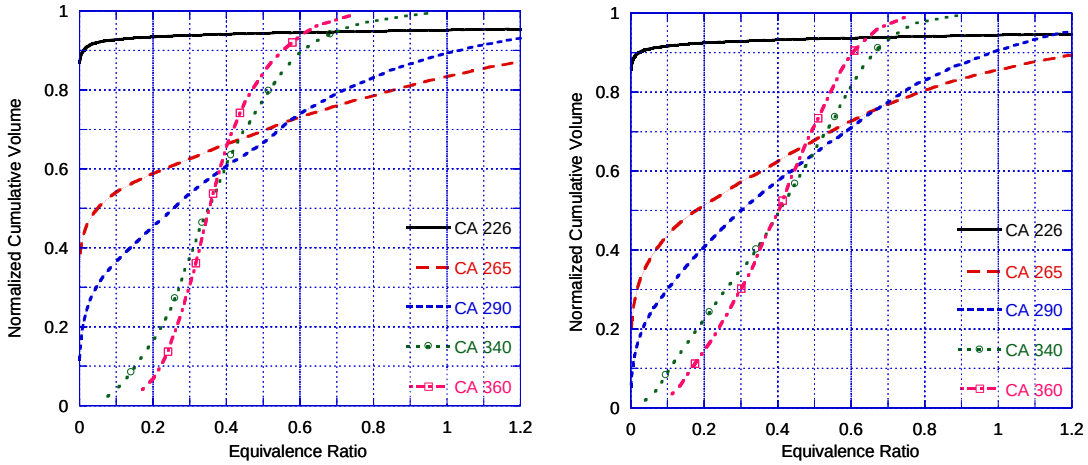

Figure 5.17 Equivalence ratio distribution at different crank angles when the injector is located between the valves
(a) Case 4: θ = 30 degrees (b) Case 5: θ = 60 degrees

When the injector is located in between the valves, results show that the jets injected at 30 degrees angle hit the piston (Case 4) whereas in the other two cases, Case 1 and Case 5, the jets impinge on the cylinder walls. The equivalence ratio distribution curves are shown in Figure 5.16 (a) and Figure 5.17. By comparing the curves of 360 ATDC for the above cases, the range of equivalence ratio is from 0.2 to 0.62 for Case 1, 0.15 to 0.75 for Case 4 and 0.10 to 0.75 for Case 5. It is seen that Case 1 has an overall steeper slope, thus indicating mixture is more homogeneous. It can also be observed that for Case 1, the percentage of the volume with equivalence ratio between 0.4 and 0.5 is approximately 28%, which is comparatively higher than

that of Case 4 (20%) and Case 5 (22%). Thus, a 45 degrees included angle of injection can result in a better fuel-air mixing when the injector is located in between the valves.

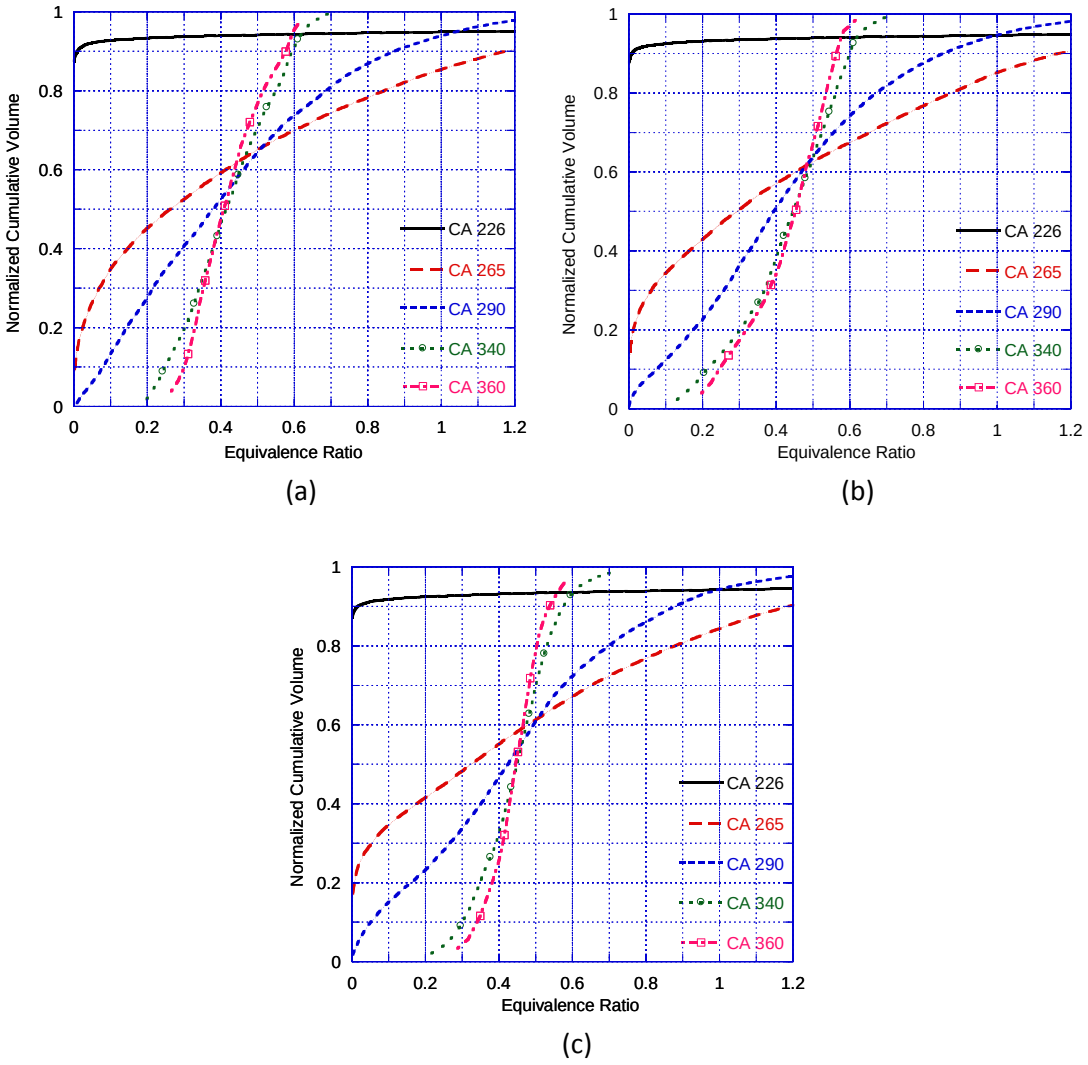

Figure 5.18 Equivalence ratio distribution at different crank angles when the injector is located near the intake valve
(a) Case 6: θ = 30 degrees (b) Case 7: θ = 45 degrees (c) Case 8: θ = 60 degrees

When the injector is located near the intake valve, the fuel jets are directed towards the center of the chamber in order to achieve a better spread of the fuel. The equivalence ratio distribution curves are shown in Figure 5.18. Results show that

the ranges of the equivalence ratio at 360 ATDC are approximately the same for all cases, but Case 8 with 60 degrees included angle can produce somewhat better mixing. With an included angle of 60 degrees, about 50% of the cylinder volume contains fuel-air mixture of equivalence ratio between 0.4 and 0.5. The corresponding percentage for 30 degrees and 45 degrees injection are 30% and 36%, respectively. Thus, a 60 degrees included angle of injection is able to render better homogeneity of fuel-air mixture when the injector is located near the intake valve.

In the third series of tests, the injector is located near the exhaust valve, symmetrically opposite to the location of the injector near the intake valve in the above cases. The injector is also directed towards the center of the chamber. It is observed that fuel jets injected at an included angle of 30 degrees are able to provide better mixing. The equivalence ratio distribution curves are shown in Figure 5.19. With an included angle of 30 degrees, about 41% of the cylinder volume contains fuel-air mixture of equivalence ratio between 0.4 and 0.5. 30% of the cylinder volume has the local equivalence ratio close to 0.45 for the injection angles of 45 degrees and 60 degrees.

In the third series of tests, the injector is located near the exhaust valve, symmetrically opposite to the location of the injector near the intake valve in the above cases. The injector is also directed towards the center of the chamber. It is observed that fuel jets injected at an included angle of 30 degrees are able to provide better mixing. The equivalence ratio distribution curves are shown in Figure 5.19. With an included angle of 30 degrees, about 41% of the cylinder volume contains fuel-air mixture of equivalence ratio between 0.4 and 0.5. 30% of the

cylinder volume has the local equivalence ratio close to 0.45 for the injection angles of 45 degrees and 60 degrees.

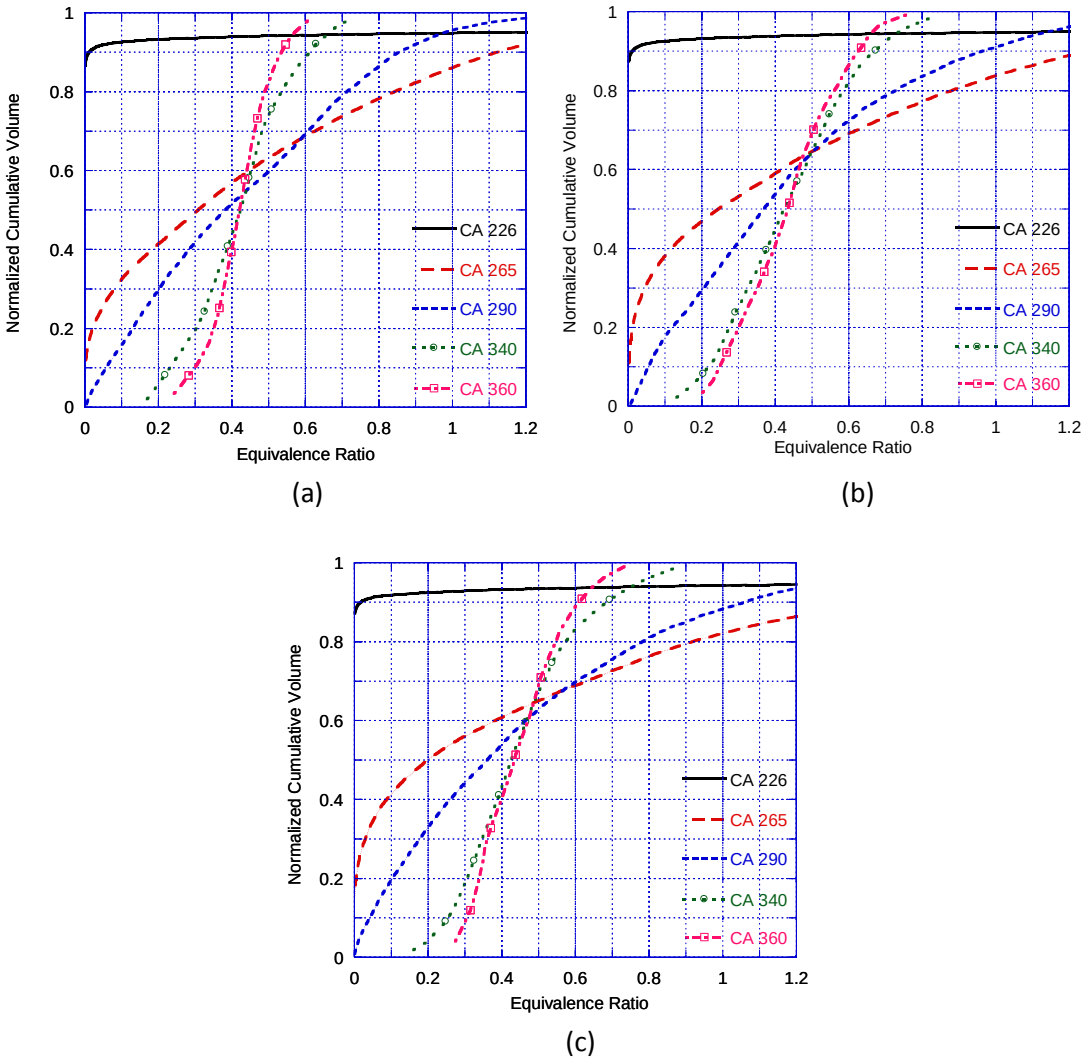

Figure 5.19 Equivalence ratio distribution at different crank angles when the injector is located near the exhaust valve
(a) Case 9: θ = 30 degrees (b) Case 10: θ = 45 degrees (c) Case 11: θ = 60 degrees

In summary, the quantitative results of the in-cylinder mixture equivalence ratio under different injection conditions are listed in Table 5.2. It is found that an early injection results in more homogeneous mixture by allowing more time for fuel-air mixing. Different injector locations require different injection angles for achieving

more homogeneous mixture since the fuel-air mixing is a result of the interaction between fuel jets and the in-cylinder flow. The favorable included injection angle is 45 degrees for the injector located between the valves, 60 degrees for the injector near the intake valve, and 30 degree for the injector near the exhaust valve. Speaking overall it is most favorable to locate the injector near the intake valve and aim towards the center of the cylinder under the present engine geometry. It is worth noting that different engine geometries will require different injection conditions to achieve desirable mixture conditions.

CHAPTER 6 CONCLUSIONS

6.1 Conclusions

A hybrid gas jet injection model was developed to simulate the high velocity gaseous hydrogen injection and mixing with air. Adaptive mesh refinement was used to provide adequate grid resolution to help capture the flow structure induced by the gas jet. The use of adaptive mesh refinement helps reduce the computer time without the loss of accuracy. The model was validated by comparing the predicted hydrogen penetrations with the experimental and theoretical data. Good levels of agreement between numerical and experimental results are obtained for single jet and multi-jet penetrations. The effect of ambient pressure is also predicted correctly. A parametric study was also conducted to explore the mixture formation characteristics inside the engine cylinder at various injection timings, injector locations, and injection angles.

The parametric study results show that the mixture distribution in the cylinder varies widely with the above three injection parameters. Results indicate that it is best to inject hydrogen soon after the intake valve closes. Such early injection can result in better homogeneity by providing more time for fuel-air mixing. Under the conditions studied, the hydrogen jets impinge on the piston surface or the cylinder wall shortly after injection. Major mixing appears to take place after the wall impingement. When the injector is located at different positions, different nozzle orientations are required to produce favorable mixture. Among all the cases studied, the injector located near the intake valve with an included injection angle of 60

degrees is able to produce the most homogeneous hydrogen-air mixture under the present engine configuration. It is anticipated that present numerical model can be used as a tool for the design of direct-injection hydrogen engines.

Recommended future study will include the implementation of premixed engine combustion models into KIVA-4 in order to simulate the entire in-cylinder process including hydrogen injection, mixing, combustion, and emissions formation. The results of combustion simulation can be compared with the experimental data on hydrogen engines. Additionally, the AMR capability of the solver will need to be enhanced in order to refine the mesh near moving surfaces. The overall numerical model can then be used as a tool to design and optimize hydrogen engines.

REFERENCES

[1] M. Ball, M. Wietschel, The future of hydrogen opportunities and challenges, Int. J. Hydrogen Energy, 34 (2009); pp. 615–627.

[2] G.A. Karim, Hydrogen as a spark ignition engine fuel, Int. J. Hydrogen Energy, 28 (2003); pp. 569-577.

[3] G.A. Karim, S.R. Klat, Hydrogen as a fuel in compression ignition engines. Journal of Mechancical Engineering ASME 98(1976); pp. 34-39.

[4] C.M. White, R.R Steeper, A.E. Lutz, The hydrogen fueled internal combustion engine:a technical review, Int. J. Hydrogen Energy, 31 (2006); pp. 1292-1305.

[5] J. Romm, The car and fuel of the future, Energy Policy, 34 (2006); pp. 2609–2614.

[6] H. Eichlseder, T. Wallner, R. Freymann, J. Ringler, The Potential of Hydrogen Internal Combustion Engines in a Future Mobility Scenario, SAE 2003-01-2267,(2003).

[7] X. Tang, D.M. Kabat, R.J. Natkin, W.F. Stockhausen, J. Heffel, Ford P2000 hydrogen engine dynamometer development, SAE Paper 2002-01-0242, (2002).

[8] A. Wimmer, T. Wallner, J. Ringler, F. Gerbig, H2-Direct Injection~A highly promising combustion concept, SAE Paper 2005-01-0108, (2005).

[9] L.M. Das, R. Gulati, P.K. Gupta, A comparative evaluation of the performance characteristics of a spark ignition engine using hydrogen and compressed natural gas as alternative fuels, Int. J. Hydrogen Energy, 25 (2000); pp. 783-793.

[10] L.M. Das, Hydrogen engine: research and development (R&D) programmes in Indian Institute of Technology (IIT) Delhi, Int. J. Hydrogen Energy, 27 (2002); pp. 953–965.

[11] H. Li, G.A. Karim, Knock in spark ignition hydrogen engines, Int. J. Hydrogen Energy, 29 (2004); pp. 859–865.

[12] A. Mohammadi, M. Shioji, Y. Nakai, W. Ishikura, E. Tabo, Performance and combustion characteristics of a direct injection SI hydrogen engine, Int. J. Hydrogen Energy, 32 (2007); pp. 296–304.

[13] T. Wallner, A.M. Nande, J. Naber, Evaluation of injector location and nozzle design in a direct-injection hydrogen research engine, SAE International 2008-01-1785, (2008).

[14] C.M. White, OH* chemiluminescence measurements in a direct injection hydrogen-fuelled internal combustion engine, Int. J. Engine Research, Vol. 8, Part 2, (2007); pp. 185-204.

[15] B.R. Peterson, J.B. Gandhi, Transient high-pressure hydrogen jet measurements, SAE International 2006-01-0652, (2006).

[16] J. Panda, R.G. Seasholts, Measurement of shock structure and shock-vortex interaction in underexpanded jets using Rayleigh scattering, Physics of Fluids, Vol. 11, No. 12, (1999); pp. 3761-3777.

[17] F.P. Ricou, D.B. Spalding, Measurement of entrainment by axisymmetrical turbulent jets, Journal of Fluid Mechanics, Vol. 11, (1961); pp. 21-32.

[18] G. N. Abramovich, The Theory of Turbulent Jets. M.I.T. Press, Massachusetts, (1963).

[19] P.O. Witze, The impulsively started incompressible turbulent jet, Sandia Laboratories Report, SAND80-8617.

[20] N. Rajaratnam, Turbulent Jets, Elsevier Scientific Publishing Company, Amsterdam, (1976).

[21] I. Wygnanski and H. Fiedler, Some measurements in the self-preserving jet, Journal of Fluid Mechanics, Vol. 38, Part 3, (1969); pp. 577-612,

[22] H. Schlichting, Boundary layer theory, fourth ed., McGraw-Hill Book Company, (1960); pp. 607-609.

[23] P. S. Cumber, M. Fairweather, S. A. E. G Falle, J.R. Giddings, Predictions of the structure of turbulent highly underexpanded jets, Journal of Fluids Engineering, 117, (1995); pp. 599-604.

[24] B.C.R Ewan, K. Moodie, Structure and velocity measurements in underexpanded jets, Combust. Sci. and Tech., 45, (1986); pp. 275-288.

[25] A. D. Birch, D. R. Brown, M. G. Dodson, and F. Swaffield, The Structure and Concentration Decay of High Pressure Jets of Natural Gas, Combustion Science and Technology, 36, (1984); pp. 249-261.

[26] J.S. Turner, The starting plume in neutral surroundings, J. Fluid Mech, 13, (1962); pp.356-368.

[27] T.W. Kuo, and F. V. Bracco, On the Scaling of Transient Laminar, Turbulent,and Spray Jets, SAE Paper 820038, (1962).

[28] S. Abramovich, A. Solan, The initial development of a submerged laminar round jet, J Fluid Mechanics, 59, (1973); pp. 791-801.

[29]H. Sato, F. Sakao, An experimental investigation of the instability of a two-dimensional jet at low Reynolds numbers, J. Fluid Mech., 20, (1964);pp. 337-352.

[30] P. Ouellette, P. G. Hill, Turbulent transient gas injections, ASME J. of Fluids Eng., vol. 122, (2000); pp. 743-751.

[31] M. Miyake, T. Biwa, Y. Endoh, M. Shimotsu, S. Murakami, S. and T. Komoda, The development of high output, highly efficient gas burning diesel engines, Paper D11.2, CIMAC Conference, Paris, 1983.

[32] J. Abraham, V. Magi, J. MacInnes, F.V. Bracco, Gas versus spray injection: which mixes faster?, SAE Paper 940895, (1994).

[33] H. Johari, Q. Zhang, M. Rose, S. Bourque, Impulsively started turbulent jets, AIAA J., 35, (1997); pp. 657-662.

[34] F. Z. Lahbabi, J. Botee, H. J. Nuglisch, and G. Charnay, Analysis of Starting and Steady Turbulent Jets by Image Processing Techniques, Experimental and Numerical Flow Visualization, ASME Fluids Engineering Division, 172, (1993); pp. 315–321.

[35] N.L. Johnson, A.A Amsden,J.D. Naber, D.L. Siebers, Three-dimensional computer modeling of hydrogen injection and combustion, Los Alamos National Laboratory Report LA-UR-95-210, (1995).

[36] Y. Li, A. Kirkpatrick,C. Mitchell, B. Willson, Characteristic and Computational Fluid Dynamics Modeling of High-Pressure Gas Jet Injection, ASME J Eng for Gas turbines and Power, 126, (2004); pp. 192-197.

[37] Y. Ra, S.C. Kong, R.D Reitz, C.J. Rutland, Multidimensional Modeling of Transient Gas Jet Injection Using Coarse Computational Grids, SAE International 2005-01-0208, (2005).

[38] D. J. Torres, Collocated KIVA-4. 11th Int. Multidimensional Engine Modelling User's Group Meeting at the SAE Congress, Detroit, Michigan, (2007).

[39] D.J. Torres, M.F. Trujillo, Kiva-4: An unstructured ALE code for compressible gas flow with sprays, J. Comp. Phys., 219, (2006); pp. 943-975.

[40] Y. Li, S.C. Kong, Mesh refinement algorithms in an unstructured solver for Multiphase flow simulation using discrete particles, J. Comp. Phys., 228, (2009); pp. 6349-6360.

[41] R.W. Anderson, N.S. Elliott, R.B. Pember, An arbitrary Lagrangian–Eulerian method with adaptive mesh refinement for the solution of the Euler equations, Journal of Computational Physics, 199 (2004); pp. 598–617.

[42] J.H. Ferziger, M. Peric, Computational Methods for Fluid Dynamics, Third edition, Springer, 2000.

[43] Y. Tsui, Y. Pan, A pressure–correction method for incompressible flows using unstructured meshes, Numerical Heat Transfer, Part B 49 (2006) ; pp. 43–65.

[44] B. E. Launder, and D. B. Spalding, The Numerical Computation of Turbulent Flow, Comp. Meth. In Appl. Mech. & Eng., 3, (1974); pp. 269.

[45] R. Scarcelli, T. Wallner, V.M. Salazar, S.A. Kaiser, Modeling and Experiments on Mixture Formation in a Hydrogen Direct-Injection Research Engine, SAE 2009-24-0083, (2009).